Astronomy & Astrophysics manuscript no. a1
June 5, 2009
© ESO 2009

arXiv:0906.1042v1 [astro-ph.CO] 5 Jun 2009

Mass function and bias of dark matter halos for non-Gaussian initial conditions

P. Valageas

Institut de Physique Théorique, CEA Saclay, 91191 Gif-sur-Yvette, France

Received / Accepted

ABSTRACT

Aims. We revisit the derivation of the mass function and the bias of dark matter halos for non-Gaussian initial conditions.
Methods. We use a steepest-descent approach to point out that exact results can be obtained for the large-mass tail of the halo mass function and the two-point correlation of massive halos. Focusing on primordial non-Gaussianity of the local type, we check that these results agree with numerical simulations.
Results. The high-mass cutoff of the halo mass function is of the same form as the one obtained from the Press-Schechter formalism, but with a linear threshold δ_L that depends on the definition of the halo (i.e. $\delta_L \simeq 1.59$ for a nonlinear density contrast of 200). We show that a simple formula, that obeys this large-mass asymptotic and uses the fit obtained for Gaussian initial conditions, matches numerical simulations while keeping the mass function normalized to unity. Next, deriving the real-space halo two-point correlation, in the spirit of Kaiser (1984), and taking a Fourier transform, we obtain a good agreement with simulations for the correction to the halo bias, $\Delta b_M(k, f_{\rm NL})$, due to primordial non-Gaussianity, without any free parameter. The nonlinear real-space expression can be useful to check that the "linearized" bias is a valid approximation. Moreover, it clearly shows how the baryon acoustic oscillation at $\sim 100h^{-1}$Mpc is amplified by the bias of massive halos and modified by primordial non-Gaussianity. At smaller scales, $30 < x < 90h^{-1}$Mpc, the correction to the real-space bias roughly scales as $f_{\rm NL}\, b_M(f_{\rm NL}=0)\, x^2$.

Key words. gravitation; cosmology: theory – large-scale structure of Universe

1. Introduction

Standard single-field slow-roll inflationary models predict a nearly scale-invariant and Gaussian spectrum of primordial curvature fluctuations (e.g., Bartolo et al. 2004). This agrees with current observations of the cosmic microwave background (CMB) anisotropies (Komatsu et al. 2008) and of large-scale structures (Slosar et al. 2008). Nevertheless, several inflationary models predict a potentially observable level of non-Gaussianity (e.g., Bartolo et al. 2004 for a review), so that constraining or detecting primordial non-Gaussianity is an important task for current cosmological studies. This would allow one to rule out some of the many inflationary models that have already been proposed. In particular, in many cases the non-Gaussianity is of the local type, meaning that it only depends on the local value of Bardeen's potential Φ. That is, the latter can be decomposed as

$$\text{local type}: \quad \Phi(\mathbf{x}) = \phi(\mathbf{x}) + f_{\rm NL}\, (\phi(\mathbf{x})^2 - \langle\phi^2\rangle), \tag{1}$$

where ϕ is a Gaussian random field. Simple slow-roll inflation gives a parameter $f_{\rm NL}$ of order 10^{-2} but this would be masked by the nonlinearities that arise from the dynamics (e.g., from the nonlinearity of Einstein's equations, see Bartolo et al. 2004) or from the physical processes involved by the observables (e.g., perturbations at recombination that affect the CMB, see Senatore et al. 2008), which give an effective $f_{\rm NL}$ of order unity. Large values of $f_{\rm NL}$ can be obtained for instance from multifield inflation (Bartolo et al. 2002; Lyth et al. 2003), self-interactions (Falk et al. 1993), tachyonic preheating in hybrid inflation (Barnaby & Cline 2006) or ghost inflation (Arkani-Hamed et al. 2004). Current limits are $-9 < f_{\rm NL} < 111$ from CMB (Komatsu et al. 2008) and $-29 < f_{\rm NL} < 70$ from large-scale structures (Slosar et al. 2008).

The effects of primordial non-Gaussianity on large-scale structures can be seen for instance through the mass function of virialized halos, especially in the large-mass tail as the steep falloff magnifies the sensitivity to initial conditions (Lucchin & Matarrese 1988; Colafrancesco et al. 1989; Grossi et al. 2007; Maggiore & Riotto 2009). This allows to use the X-ray luminosity function of clusters to constrain the amount of non-Gaussianity (Amara & Refregier 2004).

A second probe of non-Gaussianity is provided by the clustering of these halos, measured through their many-body correlations. In particular, the halo two-point correlation can be significantly increased if the underlying primordial density field is non-Gaussian (Grinstein & Wise 1986). More specifically, Dalal et al. (2008) have recently shown that primordial non-Gaussianity of the local type (1) gives rises to a strongly scale dependent bias at large scales, whereas in the Gaussian case the bias is roughly constant in this range. Thus, at linear order over $f_{\rm NL}$ they obtain in Fourier space a correction of the form

$$\Delta b_M(k, f_{\rm NL}) = f_{\rm NL}\, [b_M(k,0) - 1]\, \frac{3\delta_L \Omega_{\rm m0} H_0^2}{c^2 k^2 T(k) D(z)}, \tag{2}$$

where $b_M(k,0)$ is the Gaussian-case bias (defined as the ratio of the halo and matter power spectra, $b_M^2(k) = P_M(k)/P(k)$, for objects of mass M). Here δ_L is the linear matter density contrast associated with virialized ob-

jects (usually taken as $\delta_L \simeq 1.686$), $T(k)$ is the transfer function and $D(z)$ is the linear growth factor, normalized as $D(z) \to (1+z)^{-1}$ at high redshift. Then, Dalal et al. (2008) checked in numerical simulations that, in agreement with Eq.(2), the halo bias correction roughly grows as $1/k^2$ at low k. This gives rise to a significant and specific signal that has already been used to constrain $f_{\rm NL}$ (Slosar et al. 2008).

In this article, following a previous work devoted to the Gaussian case (Valageas 2009b), we revisit the derivations of the halo mass function and of the bias for primordial non-Gaussianity. Although we focus on the local type (1), our approach also applies to any non-Gaussian model where Bardeen's potential can be written as the sum of linear and quadratic terms over an auxiliary Gaussian field, that is, where $f_{\rm NL}$ becomes a convolution kernel (it also extends to cases that contain higher order terms and multiple Gaussian fields).

After introducing our notations and the quantities needed for our calculations in section 2, we consider the halo mass function in section 3. Here, our aim is to argue that the exponential cutoff of the large-mass tail can be obtained exactly from a saddle-point approach. This is equivalent to the saddle-point computation of Matarrese et al. (2000), that is often used to model the non-Gaussian halo mass function. However, using a different treatment, we simultaneously derive the linear density profile of this saddle-point, which allows us to check that the latter is almost insensitive to primordial non-Gaussianity, so that shell-crossing is not amplified and exact results can be obtained provided one uses the correct linear density threshold, rather than the usual one. We also propose a simple recipe to match the dependence on $f_{\rm NL}$ of the large-mass tail while keeping the mass function normalized to unity. Then, in section 4 we consider the two-point correlation of dark matter halos in real space, following the spirit of Kaiser (1984). Next, taking a Fourier transform we obtain the halo bias in Fourier space. Here, our aim is to show that one does not need to introduce free parameters to match the results of numerical simulations. Moreover, the nonlinear real-space expression is of interest by itself and it also allows one to check whether the "linearized" bias is valid on the range of interest. Finally, we conclude in section 5.

2. Non-Gaussian initial conditions

We focus in this paper on non-Gaussianities of the local type, where Bardeen's potential Φ is of the form (1), with ϕ a Gaussian random field. On scales smaller than the Hubble radius, Φ equals minus the Newtonian gravitational potential and the Poisson equation gives in Fourier space (Slosar et al. 2008)

$$\tilde{\delta}_L(\mathbf{k},z) = \alpha(k,z)\tilde{\Phi}(\mathbf{k}) \quad \text{with} \quad \alpha(k,z) = \frac{2c^2k^2T(k)D(z)}{3\Omega_{\rm m0}H_0^2}, \tag{3}$$

where δ_L is the linear matter density contrast, $T(k)$ is the transfer function and $D(z)$ is the linear growth factor, normalized as $D(z) \to (1+z)^{-1}$ at high redshift. Unless stated otherwise, we normalize the Fourier transform as

$$\delta_L(\mathbf{x}) = \int \mathrm{d}\mathbf{k}\, e^{\mathrm{i}\mathbf{k}.\mathbf{x}}\, \tilde{\delta}_L(\mathbf{k}). \tag{4}$$

Note that we define $f_{\rm NL}$ by applying Eq.(1) at early times (i.e. $z=\infty$), which is sometimes called the "CMB convention", whereas some authors first linearly extrapolate Φ at $z=0$ ("LSS convention"). Thus, both conventions are related by $f_{\rm NL}^{\rm CMB} = D(0) f_{\rm NL}^{\rm LSS}$ (Pillepich et al. 2009). Then, defining the time-dependent Gaussian field χ by

$$\tilde{\chi}(\mathbf{k},z) = \alpha(k,z)\,\tilde{\phi}(\mathbf{k}), \tag{5}$$

we can write the linear density field at redshift z as

$$\tilde{\delta}_L(\mathbf{k}) = \tilde{\chi}(\mathbf{k}) + \int \mathrm{d}\mathbf{k}_1\mathrm{d}\mathbf{k}_2\, \delta_D(\mathbf{k}_1+\mathbf{k}_2-\mathbf{k})\, \tilde{f}_{\rm NL}^{\delta}(\mathbf{k}_1,\mathbf{k}_2) \times \tilde{\chi}(\mathbf{k}_1)\,\tilde{\chi}(\mathbf{k}_2), \tag{6}$$

with

$$\text{local type}: \quad \tilde{f}_{\rm NL}^{\delta}(\mathbf{k}_1,\mathbf{k}_2) = f_{\rm NL}\,\frac{\alpha(\mathbf{k}_1+\mathbf{k}_2)}{\alpha(k_1)\,\alpha(k_2)}. \tag{7}$$

This reads in real space as

$$\delta_L(\mathbf{x}) = \chi(\mathbf{x}) + \int \mathrm{d}\mathbf{x}_1\mathrm{d}\mathbf{x}_2\, f_{\rm NL}^{\delta}(\mathbf{x};\mathbf{x}_1,\mathbf{x}_2)\,\chi(\mathbf{x}_1)\,\chi(\mathbf{x}_2), \tag{8}$$

where the kernel $f_{\rm NL}^{\delta}(\mathbf{x};\mathbf{x}_1,\mathbf{x}_2)$ only depends on the two vectors $\{\mathbf{x}_1-\mathbf{x}, \mathbf{x}_2-\mathbf{x}\}$,

$$f_{\rm NL}^{\delta}(\mathbf{x};\mathbf{x}_1,\mathbf{x}_2) = f_{\rm NL}^{\delta}(\mathbf{x}_1-\mathbf{x},\mathbf{x}_2-\mathbf{x}), \tag{9}$$

as long as the system remains statistically homogeneous, as for the local model (1). The real-space and Fourier-space kernels are related by (note the different normalization from (4))

$$f_{\rm NL}^{\delta}(\mathbf{x}_1,\mathbf{x}_2) = \int \frac{\mathrm{d}\mathbf{k}_1\mathrm{d}\mathbf{k}_2}{(2\pi)^6}\, e^{\mathrm{i}\mathbf{k}_1.\mathbf{x}_1+\mathrm{i}\mathbf{k}_2.\mathbf{x}_2}\, \tilde{f}_{\rm NL}^{\delta}(\mathbf{k}_1,\mathbf{k}_2). \tag{10}$$

The relationships (6) and (8) describe any homogeneous model where the Bardeen potential can be expressed as the sum of linear and quadratic terms over some Gaussian field. Thus, our analytical results also apply to other "$f_{\rm NL}$-type" models than the "local" one (1).

For $f_{\rm NL}=0$ we recover Gaussian initial conditions, $\delta_L = \chi$, with a linear density power spectrum

$$\langle \tilde{\chi}(\mathbf{k}_1)\tilde{\chi}(\mathbf{k}_2)\rangle = \delta_D(\mathbf{k}_1+\mathbf{k}_2)P_L(k_1), \tag{11}$$

and a two-point linear density correlation

$$C_L(\mathbf{x}_1,\mathbf{x}_2) = \langle \chi(\mathbf{x}_1)\chi(\mathbf{x}_2)\rangle = 4\pi \int \mathrm{d}k\, k^2\, P_L(k)\, \frac{\sin(k|\mathbf{x}_2-\mathbf{x}_1|)}{k|\mathbf{x}_2-\mathbf{x}_1|}. \tag{12}$$

As usual, it is convenient to introduce the smoothed linear density contrast, $\chi_q(\mathbf{x})$, within the sphere of radius q and volume V around position $\mathbf{x}$,

$$\chi_q(\mathbf{x}) = \int_V \frac{\mathrm{d}\mathbf{x}'}{V}\,\chi(\mathbf{x}+\mathbf{x}') = \int \mathrm{d}\mathbf{k}\, e^{\mathrm{i}\mathbf{k}.\mathbf{x}}\,\tilde{\chi}(\mathbf{k})\,\tilde{W}(kq), \tag{13}$$

with a top-hat window that reads in Fourier space as

$$\tilde{W}(kq) = \int_V \frac{\mathrm{d}\mathbf{x}}{V}\, e^{\mathrm{i}\mathbf{k}.\mathbf{x}} = 3\,\frac{\sin(kq)-kq\cos(kq)}{(kq)^3}. \tag{14}$$

Then, in the linear regime, the cross-correlation of the smoothed linear density contrasts at scales q_1 and q_2 and positions $\mathbf{x}_1$ and $\mathbf{x}_2 = \mathbf{x}_1 + \mathbf{x}$ reads as

$$\sigma^2_{q_1,q_2}(x) = \langle \chi_{q_1}(\mathbf{x}_1)\chi_{q_2}(\mathbf{x}_1+\mathbf{x})\rangle = 4\pi \int \mathrm{d}k\, k^2 P_L(k)\tilde{W}(kq_1)\tilde{W}(kq_2)\frac{\sin(kx)}{kx}. \quad (15)$$

In particular, $\sigma_q = \sigma_{q,q}(0)$ is the usual rms linear density contrast at scale q. Then, in the non-Gaussian case we define the initial conditions by the same power spectrum (11) for the field χ and we vary the parameter $f_{\rm NL}$ (for the local type (7)). We still define the variance σ^2 as in Eq.(15) from the Gaussian field χ.

In the following sections, where we define dark matter halos as spherical overdensities, we shall need the average of the kernel $f^\delta_{\rm NL}(\mathbf{x};\mathbf{x}_1,\mathbf{x}_2)$ over spherical cells, weighted by the linear correlation (12). Thus, omitting the superscript δ for simplicity, we define the quantity

$$f_{q;q_1,q_2}(\mathbf{x};\mathbf{x}_1,\mathbf{x}_2) = \int_V \frac{\mathrm{d}\mathbf{q}}{V}\int_{V_1}\frac{\mathrm{d}\mathbf{q}_1}{V_1}\int_{V_2}\frac{\mathrm{d}\mathbf{q}_2}{V_2}\int \mathrm{d}\mathbf{q}'_1\mathrm{d}\mathbf{q}'_2 \times f^\delta_{\rm NL}(\mathbf{q};\mathbf{q}'_1,\mathbf{q}'_2)\, C_L(\mathbf{q}'_1,\mathbf{q}_1)\, C_L(\mathbf{q}'_2,\mathbf{q}_2), \quad (16)$$

where the spheres of volumes V, V_1 and V_2, and radii q, q_1 and q_2, are centered on the points $\mathbf{x}$, $\mathbf{x}_1$ and $\mathbf{x}_2$. In Eq.(16) the coordinates $\mathbf{q}'_1$ and $\mathbf{q}'_2$ are integrated over all space. In terms of the Fourier kernel $\tilde{f}^\delta_{\rm NL}$ this reads as

$$f_{q;q_1,q_2}(\mathbf{x};\mathbf{x}_1,\mathbf{x}_2) = \int \mathrm{d}\mathbf{k}_1\mathrm{d}\mathbf{k}_2\, \tilde{f}^\delta_{\rm NL}(\mathbf{k}_1,\mathbf{k}_2)\, P_L(k_1)P_L(k_2) \times \tilde{W}(k_1q_1)\,\tilde{W}(k_2q_2)\,\tilde{W}(|\mathbf{k}_1+\mathbf{k}_2|q) \times e^{\mathrm{i}\mathbf{k}_1.(\mathbf{x}_1-\mathbf{x})+\mathrm{i}\mathbf{k}_2.(\mathbf{x}_2-\mathbf{x})}. \quad (17)$$

Thanks to statistical homogeneity and isotropy, the kernel $\tilde{f}^\delta_{\rm NL}(\mathbf{k}_1,\mathbf{k}_2)$ only depends on the lengths k_1, k_2, and on the angle between both vectors. Then, for spheres that are centered on the same point (i.e. $\mathbf{x} = \mathbf{x}_1 = \mathbf{x}_2$), Eq.(17) simplifies as

$$\mathbf{x}=\mathbf{x}_1=\mathbf{x}_2: \quad f_{q;q_1,q_2} = 8\pi^2\int_0^\infty \mathrm{d}k_1\, k_1^2 P_L(k_1)\tilde{W}(k_1q_1) \times \int_0^\infty \mathrm{d}k_2\, k_2^2 P_L(k_2)\tilde{W}(k_2q_2)\int_{-1}^1 \mathrm{d}\mu\, \tilde{W}(kq)\tilde{f}^\delta_{\rm NL}(k_1,k_2,\mu), \quad (18)$$

which does not depend on the position $\mathbf{x}$ of the sphere. Here we defined $\mu = (\mathbf{k}_1.\mathbf{k}_2)/(k_1k_2)$, and $k^2 = k_1^2+k_2^2+2k_1k_2\mu$. On the other hand, when we consider the two-point correlation of dark matter halos, the three spheres in Eq.(16) are chosen among two possible spheres V_a and V_b, separated by a distance x. Then, we need the two quantities,

$$V = V_a,\ V_1 = V_2 = V_b: \quad f_{a;bb}(x) = 8\pi^2\int_0^\infty \mathrm{d}k_1\, k_1^2 P_L(k_1) \times\tilde{W}(k_1q_b)\int_0^\infty \mathrm{d}k_2\, k_2^2 P_L(k_2)\tilde{W}(k_2q_b) \times \int_{-1}^1 \mathrm{d}\mu\, \tilde{W}(kq_a)\tilde{f}^\delta_{\rm NL}(k_1,k_2,\mu)\frac{\sin(kx)}{kx}, \quad (19)$$

and

$$V_1 = V_a,\ V = V_2 = V_b: \quad f_{b;ab}(x) = 8\pi^2\int_0^\infty \mathrm{d}k_1\, k_1^2 P_L(k_1) \times\tilde{W}(k_1q_a)\frac{\sin(k_1x)}{k_1x}\int_0^\infty \mathrm{d}k_2\, k_2^2 P_L(k_2)\tilde{W}(k_2q_b) \times \int_{-1}^1 \mathrm{d}\mu\, \tilde{W}(kq_b)\tilde{f}^\delta_{\rm NL}(k_1,k_2,\mu). \quad (20)$$

Their Fourier transforms with respect to the separation $\mathbf{x}$ read as

$$\tilde{f}_{a;bb}(k) = \int \mathrm{d}\mathbf{k}_1\mathrm{d}\mathbf{k}_2\,\delta_D(\mathbf{k}_1+\mathbf{k}_2-\mathbf{k})P_L(k_1)P_L(k_2) \times\tilde{W}(k_1q_b)\tilde{W}(k_2q_b)\tilde{W}(kq_a)\tilde{f}^\delta_{\rm NL}(\mathbf{k}_1,\mathbf{k}_2), \quad (21)$$

and

$$\tilde{f}_{b;ab}(k) = P_L(k)\tilde{W}(kq_a)\int \mathrm{d}\mathbf{k}_1\, P_L(k_1)\tilde{W}(k_1q_b) \times\tilde{W}(|\mathbf{k}_1+\mathbf{k}|q_b)\tilde{f}^\delta_{\rm NL}(\mathbf{k},\mathbf{k}_1). \quad (22)$$

3. Mass function of dark matter halos

We now extend the analysis of Valageas (2009b) to obtain the mass function of dark matter halos for non-Gaussian initial conditions.

3.1. Rare-event saddle point for the density distribution

In a fashion similar to Valageas (2009b), we note that the exponential falloffs of the large-mass tail of the halo mass function $n(M)$, and of the overdensity tail of the linear density contrast distribution $\mathcal{P}_L(\delta_{Lq})$, can be exactly obtained from the constrained maximum,

$$\text{rare events}: \quad \mathcal{P}_L(\delta_L) \sim \max_{\{\chi[\mathbf{q}]|\delta_{Lq}=\delta_L\}} e^{-\frac{1}{2}\chi.C_L^{-1}.\chi}. \quad (23)$$

Here we introduced the probability distribution $\mathcal{P}_L(\delta_{Lq})$ of the smoothed linear density contrast within the sphere of radius q, which we can take centered on the origin,

$$\delta_{Lq} = \int_V \frac{\mathrm{d}\mathbf{q}'}{V}\,\delta_L(\mathbf{q}') = \int \mathrm{d}\mathbf{k}\,\tilde{\delta}_L(\mathbf{k})\,\tilde{W}(kq). \quad (24)$$

In the Gaussian case, $f_{\rm NL} = 0$, we simply have $\delta_{Lq} = \chi_q$, as defined in Eq.(13), and the probability distribution $\mathcal{P}_L$ is a Gaussian. Then, as stressed in Valageas (2009a,b), in the limit of rare events (e.g., at fixed density contrast δ_{Lq} in the large-scale or large-mass limit $q\to\infty$), the tails of the distribution $\mathcal{P}_L$ are obtained from Eq.(23), where we maximize the statistical weight $e^{-(\chi.C_L^{-1}.\chi)/2}$ of the Gaussian field χ, under the constraint that the smoothed linear density contrast δ_{Lq} is equal to the value of interest. Equation (23) only gives the leading-order exponential falloff. Subleading terms, such as power-law prefactors, may be obtained by expanding around the saddle-point χ, within a steepest-descent method. This also provides the probability distribution $\mathcal{P}(\delta)$ of the nonlinear density contrast δ at scale r in the quasi-linear regime, as well as the cumulant generating function (Valageas 2002a,b; 2009a,b)[1]. As pointed out in

[1] As shown in Valageas (2009a), for the closely related adhesion model, where the same procedure can be applied, one can explicitly check that the asymptotic results obtained by this approach agree with the complete distribution $\mathcal{P}(\delta)$ that is exactly known for two cases (Brownian and white-noise linear velocity in 1-D, corresponding to a power-law linear density power spectrum with $n=-2$ and $n=0$).

Valageas (2009b), this also gives the large-mass tail of the halo mass function, if halos are defined as spherical overdensities with a fixed nonlinear density threshold δ_r. Then, the halo mass M and radius r are related to the Lagrangian radius q and linear density threshold δ_{Lq} through

$$q^3 = (1+\delta_r)\, r^3, \quad \text{with} \quad \delta_r = \mathcal{F}(\delta_{Lq}), \tag{25}$$

and

$$M = \overline{\rho}_{\rm m} \frac{4\pi}{3} q^3, \tag{26}$$

where the function $\mathcal{F}$ describes the spherical collapse dynamics. This holds as long as shell-crossing has not extended beyond radius r, so that the usual spherical collapse dynamics at constant mass is valid. This yields an upper bound δ_+ for the nonlinear density threshold that can be used to define halos to take advantage of the exact asymptotic tail (23). For the preferred ΛCDM model this gives $\delta_+ \sim 200$ for $M \sim 10^{15} h^{-1} M_\odot$ up to $\delta_+ \sim 600$ for $M \sim 10^{11} h^{-1} M_\odot$ (the dependence on mass is due to the change of slope of the matter power spectrum $P_L(k)$).

In the Gaussian case, the constrained weight (23) simply reads as $e^{-\delta_{Lq}^2/(2\sigma_q^2)}$, and we recover the exponential tail of the usual Press-Schechter mass function (Press & Schechter 1974), except that the standard threshold $\delta_c \simeq 1.686$ must be replaced by $\delta_L = \mathcal{F}^{-1}(\delta)$, with $\delta_L \simeq 1.59$ for $\delta = 200$. In the non-Gaussian case, that is for $f_{\rm NL} \neq 0$, we can compute the weight (23) by using a Lagrange multiplier λ. Thus, we define the action $\mathcal{S}[\chi, \lambda]$,

$$\mathcal{S}[\chi,\lambda] = \lambda\, (\delta_L - \delta_{Lq}[\chi]) + \frac{1}{2}\, \chi . C_L^{-1} . \chi \tag{27}$$

where $\delta_{Lq}[\chi]$ is the nonlinear functional that affects to the initial condition defined by the Gaussian field χ the linear density contrast δ_{Lq} within the sphere of radius q, obtained through Eq.(8). Then, we must look for the saddle-point of the action (27), with respect to both χ and λ. Thus, differentiating the action (27) with respect to $\chi(\mathbf{q})$ and multiplying by the operator C_L gives

$$\chi(\mathbf{q}) = \lambda\, C_L(\mathbf{q},\mathbf{q}') . \frac{\mathcal{D}\delta_{Lq}}{\mathcal{D}\chi(\mathbf{q}')}, \tag{28}$$

whence, using Eq.(8),

$$\chi(\mathbf{q}) = \lambda \int_V \frac{{\rm d}\mathbf{q}'}{V}\, C_L(\mathbf{q},\mathbf{q}') + 2\lambda \int_V \frac{{\rm d}\mathbf{q}'}{V} \int {\rm d}\mathbf{q}_1 {\rm d}\mathbf{q}_2 \times f_{\rm NL}^{\delta}(\mathbf{q}';\mathbf{q}_1,\mathbf{q}_2)\, C_L(\mathbf{q},\mathbf{q}_2)\, \chi(\mathbf{q}_1). \tag{29}$$

Differentiating the action (27) with respect to λ gives the constraint

$$\delta_L = \delta_{Lq}[\chi], \tag{30}$$

whence

$$\delta_L = \int_V \frac{{\rm d}\mathbf{q}}{V} \left[\chi(\mathbf{q}) + \int {\rm d}\mathbf{q}_1 {\rm d}\mathbf{q}_2\, f_{\rm NL}^{\delta}(\mathbf{q};\mathbf{q}_1,\mathbf{q}_2)\, \chi(\mathbf{q}_1)\, \chi(\mathbf{q}_2) \right]. \tag{31}$$

Next, we solve the system (29)-(31) as a perturbative series over the non-Gaussianity kernel $f_{\rm NL}^{\delta}$ (i.e. over powers of the parameter $f_{\rm NL}$). At order zero we recover the Gaussian saddle-point,

$$\chi^{(0)}(\mathbf{q}) = \lambda^{(0)} \int_V \frac{{\rm d}\mathbf{q}'}{V}\, C_L(\mathbf{q},\mathbf{q}'), \tag{32}$$

$$\lambda^{(0)} = \frac{\delta_L}{\sigma_q^2}. \tag{33}$$

At first order we obtain

$$\chi^{(1)}(\mathbf{q}) = \lambda^{(1)} \int_V \frac{{\rm d}\mathbf{q}'}{V}\, C_L(\mathbf{q},\mathbf{q}') + 2\lambda^{(0)2} \int_V \frac{{\rm d}\mathbf{q}' {\rm d}\mathbf{q}_1'}{V^2} \times \int {\rm d}\mathbf{q}_1 {\rm d}\mathbf{q}_2\, f_{\rm NL}^{\delta}(\mathbf{q}';\mathbf{q}_1,\mathbf{q}_2)\, C_L(\mathbf{q},\mathbf{q}_2)\, C_L(\mathbf{q}_1,\mathbf{q}_1'), \tag{34}$$

$$\lambda^{(1)} = -3\, \frac{\delta_L^2}{\sigma_q^6}\, f_{q;qq}, \tag{35}$$

where the quantity $f_{q;qq}$ is given by Eq.(18).

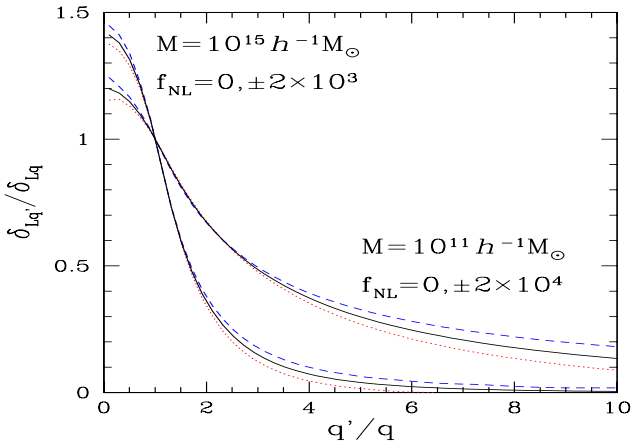

Fig. 1. The radial profile (36)-(37) of the linear density contrast $\delta_{Lq'}$ of the saddle point of the action $\mathcal{S}[\chi,\lambda]$. We show the profiles obtained with a ΛCDM cosmology for the masses $M = 10^{11}$ and $10^{15} h^{-1} M_\odot$. A larger mass corresponds to a lower ratio $\delta_{Lq'}/\delta_{Lq}$ at large radii $q'/q > 1$. We show our results for the Gaussian case (solid line), positive $f_{\rm NL}$ (dashed line) and negative $f_{\rm NL}$ (dotted line), for the local model (7).

From Equations (32)-(35) we also obtain the radial linear density profile of the saddle-point, up to first order,

$$\delta_{Lq'}^{(0)} = \frac{\delta_L}{\sigma_q^2}\, \sigma_{q,q'}^2, \tag{36}$$

$$\delta_{Lq'}^{(1)} = \frac{\delta_L^2}{\sigma_q^4} \left[f_{q';qq} + 2 f_{q;qq'} - 3 \frac{\sigma_{q,q'}^2}{\sigma_q^2} f_{q;qq} \right]. \tag{37}$$

We can check that at $q' = q$ it verifies the constraint (30), and at order zero we recover the Gaussian profile (Valageas 2009b). Equations (36)-(37) give the integrated density profile, that is, $\delta_{Lq'}$ is the mean linear density contrast within the Lagrangian radius q'. The local linear density contrast at radius q', $\delta_L(q')$, is given by

$$3 q'^3 \delta_L(q') = \frac{\partial}{\partial q'} (q'^3 \delta_{Lq'}), \tag{38}$$

whence

$$\delta_L^{(0)}(q') \;=\; \frac{\delta_L}{\sigma_q^2}\,\sigma^2_{q,0}(q'), \tag{39}$$

$$\delta_L^{(1)}(q') \;=\; \frac{\delta_L^2}{\sigma_q^4}\left[f_{0;qq}(q') + 2f_{q;0q}(q') - 3\frac{\sigma^2_{q,0}(q')}{\sigma_q^2}f_{q;qq}\right] \tag{40}$$

where $f_{0;qq}(q')$ and $f_{q;0q}(q')$ are given by Eqs.(19)-(20).

We show in Fig. 1 the integrated linear density profile (36)-(37) obtained for the masses $M = 10^{11}$ and $10^{15}h^{-1}M_\odot$, for a ΛCDM cosmology. The dependence on mass is due to the change of slope of the linear power spectrum with scale. We plot our results for the Gaussian case ($f_{\rm NL} = 0$, solid lines), large positive $f_{\rm NL}$ ($f_{\rm NL} = 2\times10^3$ and $f_{\rm NL} = 2\times10^4$, dashed lines) and large negative $f_{\rm NL}$ ($f_{\rm NL} = -2\times10^3$ and $f_{\rm NL} = -2\times10^4$, dotted lines), for the local model (7). Thus, we can see that a positive $f_{\rm NL}$ increases the relative density (i.e. with respect to the density at radius q) both at small and large radii. The very large values of $f_{\rm NL}$ required to be able to distinguish the curves in the figure imply that for realistic cases ($|f_{\rm NL}| < 100$) the perturbation of the density profile is very small. Therefore, the values of the upper boundary δ_+, which marks the onset of shell-crossing, obtained in Valageas (2009b) for the Gaussian case remain valid up to a very good accuracy. We can note that to obtain a similar deviation from the Gaussian profile we need a larger value of the parameter $f_{\rm NL}$ at smaller scale. This can be understood from the expression (7), which scales as $\tilde{f}^\delta \sim f_{\rm NL}/\alpha(k) \propto f_{\rm NL}/(k^2T(k))$ and grows as k^{-2} at very large scales. The same behavior (i.e. a higher sensitivity to local-type non-Gaussianity at large scales) is obtained for the bias of dark matter halos, see Eq.(2) above and section 4 below.

Next, we define the constrained weight (23) as

$$\Gamma = \frac{1}{2}\chi.C_L^{-1}.\chi \tag{41}$$

at the relevant saddle-point χ. This gives, up to first order,

$$\Gamma^{(0)} \;=\; \frac{1}{2}\chi^{(0)}.C_L^{-1}.\chi^{(0)} = \frac{\delta_L^2}{2\sigma_q^2}, \tag{42}$$

$$\Gamma^{(1)} \;=\; \chi^{(0)}.C_L^{-1}.\chi^{(1)} = -\,\frac{\delta_L^3}{\sigma_q^6}\,f_{q;qq}. \tag{43}$$

Therefore, the tails of the probability distribution (23) read as

$$\mathcal{P}_L(\delta_L) \sim e^{-\frac{\delta_L^2}{2\sigma_q^2}+\frac{\delta_L^3}{\sigma_q^6}f_{q;qq}} = e^{-\frac{\delta_L^2}{2\sigma_q^2}\left(1-\frac{\delta_L}{3}S_3^{(1)}\right)}, \tag{44}$$

where we introduced the skewness of the linear density contrast, at first order over $f_{\rm NL}$,

$$S_3^{(1)} = \left[\frac{\langle\delta_{Lq}^3\rangle}{\langle\delta_{Lq}^2\rangle^2}\right]^{(1)} = 6\,\frac{f_{q;qq}}{\sigma_q^4}. \tag{45}$$

Indeed, from Eq.(8) we have at first order

$$\langle\delta_{Lq}^3\rangle^{(1)} \;=\; 3\int_V \frac{{\rm d}\mathbf{q}_1{\rm d}\mathbf{q}_2{\rm d}\mathbf{q}_3}{V^3}\int {\rm d}\mathbf{q}_1'{\rm d}\mathbf{q}_2'\,f_{\rm NL}^\delta(\mathbf{q}_3;\mathbf{q}_1'\mathbf{q}_2') \times\langle\chi(\mathbf{q}_1)\chi(\mathbf{q}_2)\chi(\mathbf{q}_1')\chi(\mathbf{q}_2')\rangle \tag{46}$$

$$\;=\; 6\,f_{q;qq}. \tag{47}$$

Hereafter, since $S_3^{(0)} = 0$, we simply note $S_3 = S_3^{(1)}$.

3.2. Mass function

Following the Press-Schechter approach (Press & Schechter 1974), the mass function that is obtained in the Gaussian case from the probability distribution $\mathcal{P}_L(\delta_{Lq})$ reads as

$$n(M, f_{\rm NL}=0){\rm d}M = \frac{\overline{\rho}_{\rm m}}{M}f(\nu)\frac{{\rm d}\nu}{\nu}, \tag{48}$$

with (using the subscript "PS" to distinguish the Press-Schechter prediction)

$$f_{\rm PS}(\nu) = \sqrt{\frac{2}{\pi}}\,\nu\,e^{-\nu^2/2} \tag{49}$$

and

$$\nu = \frac{\delta_L}{\sigma(M)}. \tag{50}$$

Here $\sigma(M) = \sigma_q$, where the Lagrangian scale q is related to M by Eq.(26). As stressed in Valageas (2009b), the linear threshold δ_L in Eq.(50) must be defined as $\mathcal{F}^{-1}(\delta)$, as in Eq.(25), which gives $\delta_L \simeq 1.59$ for $\delta = 200$. Then, the exponential tail of (49) is exact,

$$\nu\to\infty: \;\; \ln[f(\nu)] \sim -\frac{\nu^2}{2}, \tag{51}$$

but the power-law prefactor and the low-mass tail of (49) have no reason to be valid (and numerical simulations indeed show that they are not exact). Then, in order to match numerical simulations, one needs to use fitting formulae. One such fit to simulations, which obeys the exact tail (51), is (Valageas 2009b)

$$f(\nu) = 0.5\left[(0.6\,\nu)^{2.5} + (0.62\,\nu)^{0.5}\right]\,e^{-\nu^2/2}. \tag{52}$$

Both mass functions (49) and (52) satisfy the normalization

$$\int_0^\infty \frac{{\rm d}\nu}{\nu}\,f(\nu) = 1, \tag{53}$$

which ensures that all the mass is contained in such halos:

$$\int_0^\infty M\,n(M){\rm d}M = \overline{\rho}_{\rm m}. \tag{54}$$

In the non-Gaussian case, that is $f_{\rm NL} \neq 0$, we may estimate the halo mass function by multiplying the Gaussian one by the corrective factor obtained in Eq.(44),

$$f_{\rm NL}\neq0: \;\; n(M, f_{\rm NL}) = n(M,0)\,e^{S_3\delta_L^3/(6\sigma_q^2)}. \tag{55}$$

As explained above, this yields the exact large-mass tail (up to first order over $f_{\rm NL}$) but it is not expected to hold for the low-mass tail. In particular, this gives a non-Gaussian mass function that does not obey the normalization (54). In order to satisfy Eq.(54), while keeping the large-mass tail of Eq.(55), a simple procedure is to make use of the scaling (48) and of the normalization (53). Thus, modifying the relationship (50) as (see Eq.(44))

$$\mu = \frac{\delta_L}{\sigma(M)}\sqrt{1-\frac{\delta_L}{3}S_3(M)}, \tag{56}$$

we may use for the non-Gaussian mass function

$$f_{\rm NL}\neq0: \;\; n(M, f_{\rm NL}){\rm d}M = \frac{\overline{\rho}_{\rm m}}{M}f(\mu)\frac{{\rm d}\mu}{\mu}, \tag{57}$$

where we use the same scaling function f as for the Gaussian case (48). This recovers the large-mass tail (55) and satisfies the normalization (54). Note that Afshordi & Tolley (2009) have recently proposed a similar rescaling as (56), which they re-interprate as a modified effective variance σ_q^2. However, to obtain such a rescaling they use some approximations, such as the decoupling between the local values of the fields $\phi(\mathbf{x})$ and $\chi(\mathbf{x})$, in the spirit of a peak-background split approximation, whereas the derivation presented here is asymptotically exact. Equation (57) yields for the ratio of both mass functions at fixed mass M,

$$\frac{n(M,f_{\rm NL})}{n(M,0)} = \frac{f(\mu)/\mu}{f(\nu)/\nu}\,\frac{{\rm d}\mu}{{\rm d}\nu}. \tag{58}$$

Using Eqs.(50), (56), we obtain

$$\frac{{\rm d}\mu}{{\rm d}\nu} = \sqrt{1-\frac{\delta_L}{3}S_3} + \frac{\sigma\,\delta_L}{6\sqrt{1-\frac{\delta_L}{3}S_3}}\,\frac{{\rm d}S_3}{{\rm d}\sigma}. \tag{59}$$

If we use the Press-Schechter mass function (49), Eqs.(57)-(59) give back the result obtained in Matarrese et al. (2000), except for the fact that we use $\delta_L \simeq 1.59$ instead of 1.686 as explained above.

Note that Matarrese et al. (2000) also use a saddle-point approach to derive the halo mass function for non-Gaussian initial conditions, expanding at linear order over $f_{\rm NL}$ (or S_3), so that their computation is equivalent to the one described above. However, since they first compute the cumulant generating function ($W(\lambda)$ in their notations, or $\varphi(y)$ in Valageas 2009b), the constraint (30) is expressed through a Dirac function, written as an exponential by introducing an auxiliary variable λ, so that they can first integrate over the Gaussian field χ and next expand over $f_{\rm NL}$ the expression obtained for $W(\lambda)$. The somewhat simpler method described in this article has the advantage of simultaneously giving the density profile (36)-(37) of the underlying saddle-point. As explained above in Fig. 1, this allows us to check that realistic amounts of primordial non-Gaussianity have a negligible effect on this profile, so that the onset of shell-crossing appears for almost the same nonlinear density threshold δ_+. This ensures that the rare-event and large-mass tails (44) and (55) are exact (at leading order), as long as halos are defined by a nonlinear threshold $\delta \sim 200$ below the upper bound δ_+. The simplicity of the method presented in this article also allows a straightforward application to two-point distributions, as shown in section 4 below, or to more complex primordial non-Gaussianities, that may involve several fields or higher-order polynomials as in Eq.(95) below.

Another approach presented in Lo Verde et al. (2008) is to use the Edgeworth expansion, that writes the probability distribution $\mathcal{P}_L(\delta_L)$ as a series over the cumulants of the non-Gaussian variable δ_L. In practice, one truncates at the lowest order beyond the Gaussian, that is, at the third cumulant $\langle\delta_L^3\rangle_c$ described by S_3. Thus, expanding the exponentials (44) and (55) one recovers the results of Lo Verde et al. (2008) at large ν (i.e. low σ_q). However, in the rare-event limit, where computations rest on firm grounds as explained above, the Edgeworth expansion does not fare very well. In particular, although we only derived the saddle-point χ and the argument Γ of the exponential up to linear order over $f_{\rm NL}$, see Eqs.(42)-(43), it is best to keep the exponential as in Eqs.(55) or (57). Indeed, in the rare-event and small-$f_{\rm NL}$ limits, the tail (55) can be a good approximation even when the corrective factor $S_3\delta_L^3/(6\sigma_q^2)$ is much larger than unity (i.e. we can have the hierarchy $\Gamma^{(0)} \gg \Gamma^{(1)} \gg 1 \gg \Gamma^{(2)}$).

Since the low-mass tail (49) does not match numerical simulations, it is sometimes proposed to keep the ratio (58) given by the Press-Schechter mass function, and to multiply the fit from simulations of the Gaussian mass function by this factor (Grossi et al. 2007, 2009; Lo Verde et al. 2008). However, this procedure clearly violates the normalization condition (54). Therefore, we suggest to use (58) with the fitting formula obtained from Gaussian simulations, that is, to use Eq.(57), which automatically satisfies the normalization (54). However, there is no reason to expect that the low-mass tail can be exactly recovered by any such procedure, even though by construction it gives the right behavior for the Gaussian case, as the low-mass slope might also depend on $f_{\rm NL}$ in some specific manner.

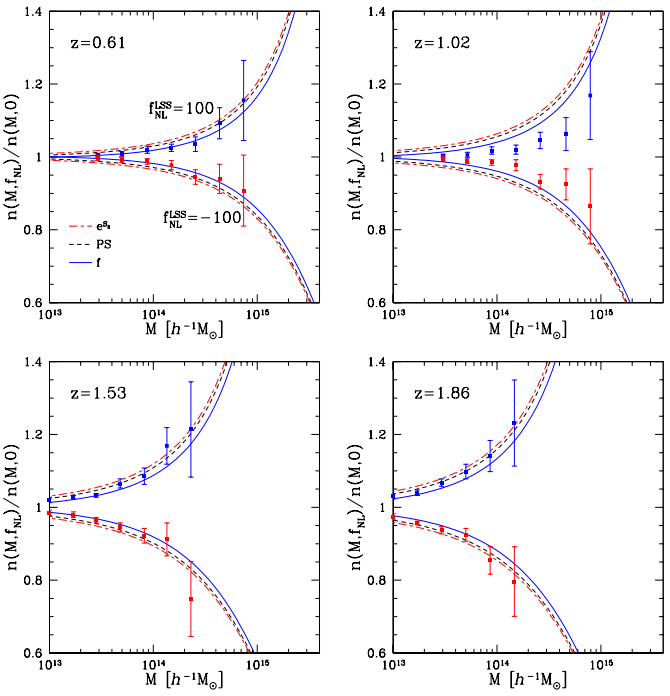

Fig. 2. The ratio $n(M,f_{\rm NL})/n(M,0)$, of the mass functions obtained for $f_{\rm NL}^{\rm LSS} = \pm 100$ over the mass function obtained for Gaussian initial conditions, as a function of M for several redshifts. The dot-dashed line labeled "e^{S_3}" is the multiplicative factor (55), the dashed line labeled "PS" is Eq.(58) with the Press-Schechter mass function (44), which also corresponds to the result of Matarrese et al. (2000) (but with $\delta_L \simeq 1.59$), the solid line labeled "f" is Eq.(58) with the fitting function (52). The data points are the results from the numerical simulations of Grossi et al. (2009).

We compare in Figs. 2, 3, our results for the halo mass function with numerical simulations from Grossi et al. (2009). Note that they use the LSS convention for $f_{\rm NL}$, so that in terms of the CMB convention used in this article this corresponds to $f_{\rm NL} \simeq \pm 75$ (Fig. 2) and $f_{\rm NL} \simeq \pm 151$ (Fig. 3). We show the ratio of the non-Gaussian mass function to the Gaussian one, as given by the multiplicative factor (55) (dot-dashed line), the ratio (58) computed with

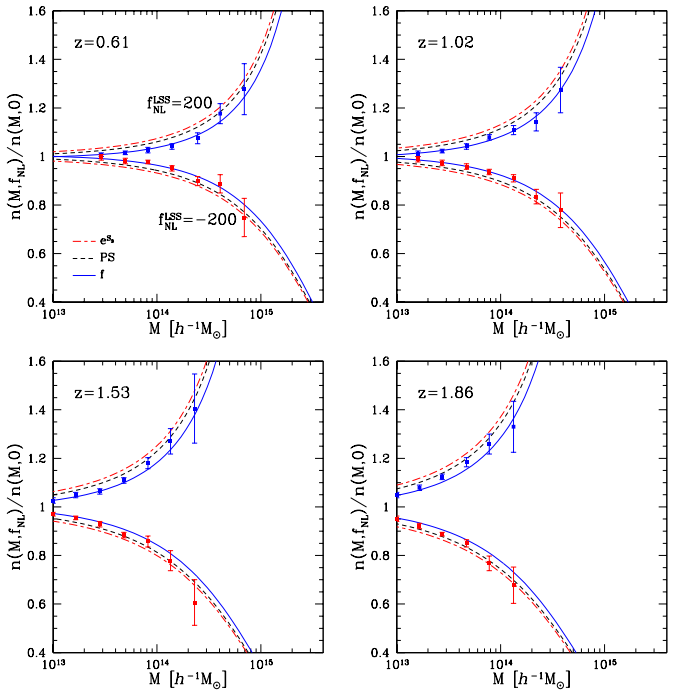

Fig. 3. Same as Fig. 2 but with $f_{\rm NL}^{\rm LSS} = \pm 200$.

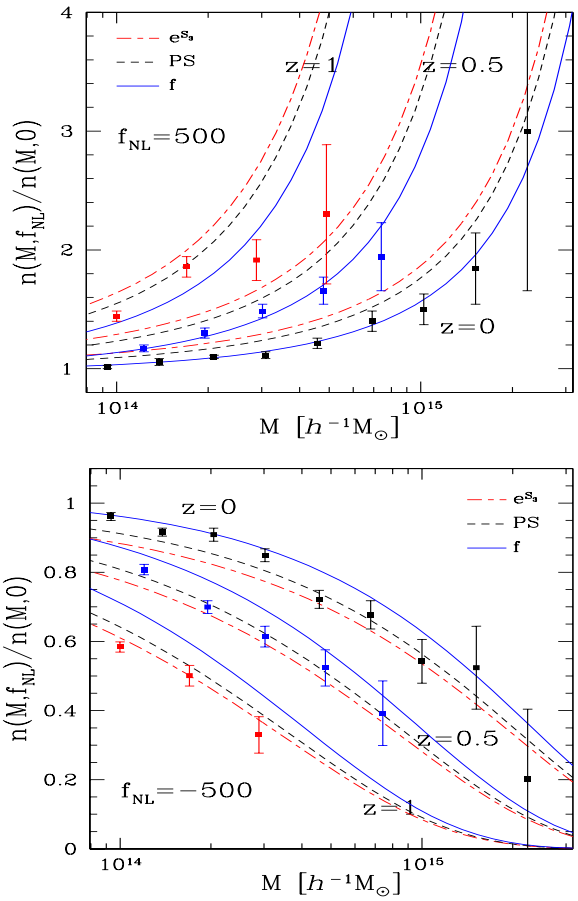

Fig. 4. Same as Fig. 2, but with $f_{\rm NL} = 500$ (upper panel) and $f_{\rm NL} = -500$ (lower panel). The data points are the results from the numerical simulations of Dalal et al. (2008).

the Press-Schechter mass function (44) (dashed line) or with the fitting function (52) (solid line). In agreement with Grossi et al. (2009), we find that the ratio (58) computed with the Press-Schechter mass function, which also corresponds to the result of Matarrese et al. (2000) (but with $\delta_L \simeq 1.59$ instead of 1.686 as explained above), agrees reasonably well with simulations. Using the fitting function (52), or the simple multiplicative factor (55), yields close results in this regime and also agrees with simulations. However, using Eq.(58) with the fitting function (52) appears to give a somewhat better agreement with simulations, especially at low masses. This could be expected from the fact that this procedure ensures that the mass function is properly normalized (by contrast, the simple multiplicative factor (55) is larger than unity and does not reproduce the crossing of both mass functions for $\nu \sim 1$).

Next, we compare in Fig. 4 our results with numerical simulations from Dalal et al. (2008). We again show the ratio $n(M, f_{\rm NL})/n(M, 0)$ as a function of mass, but for a larger primordial non-Gaussianity, $f_{\rm NL} = \pm 500$. For $f_{\rm NL} = 500$ (upper panel) we note as in Dalal et al. (2008) that the prediction of (58) computed with the Press-Schechter mass function (44) (i.e. the result of Matarrese et al. 2000 but with $\delta_L \simeq 1.59$) tends to overestimate the deviations from the Gaussian case (and the simple multiplicative factor (55) fares somewhat worse). However, using Eq.(58) with the correct Gaussian mass function (52) decreases somewhat this ratio (as in Figs. 2, 3) and provides a good agreement with the simulations. For $f_{\rm NL} = -500$ (lower panel) the match is not so good. However, in the latter case the agreement might improve at higher masses, where there are no data points but where the predictions (55) or (58) are asymptotically exact. Moreover, we can note that the discrepancy between theoretical predictions and numerical simulations is of the same order as the deviation between the different theoretical curves. Since the latter share the same exact large-mass behavior (at the leading order given by the exponential cutoff (44)), these deviations show the sensitivity of the mass functions to the details of the theoretical prescriptions. Note that these power-law prefactors have not been rigorously derived (and are expected not to be exact, for all formulae used here). Therefore, the deviation between these theoretical predictions gives an estimate of the theoretical uncertainty for the ratio of the halo mass functions. Then, taking into account this theoretical uncertainty, we can see that the agreement with the numerical results is still reasonable. For practical purposes, when one tries to derive constraints on cosmology from observations of halo mass functions, it would be useful to consider several theoretical prescriptions in addition to the best prediction (58)-(52), as in Figs. 2-Fig. 4, so as to take into account the theoretical uncertainty in the analysis.

4. Bias of dark matter halos

4.1. Two-cells saddle-point and real-space bias

We now consider the bias of dark matter halos, or more precisely their two-point correlation function. As in Valageas (2009b), following Kaiser (1984), since we identify rare massive halos with positive density fluctuations in the linear density field, we first consider the bivariate probability distribution, $\mathcal{P}_L(\delta_{L1}, \delta_{L2})$, of the linear density contrasts δ_{L1}

and δ_{L2} within two spheres V_1 and V_2, of radii q_1 and q_2, and separated by the distance s. Note that we distinguish the Lagrangian distance s between the halos, measured in the linear density field, from their Eulerian distance x, measured in the nonlinear density field. Indeed, since halos have moved through their mutual gravitational attraction these two distances are usually different. Proceeding as in section 3.1, to obtain the rare-event tails,

$$\mathcal{P}_L(\delta_{L1},\delta_{L2}) \sim \max_{\{\chi[\mathbf{q}]|\delta_{Lq1}=\delta_{L1},\delta_{Lq2}=\delta_{L2}\}} e^{-\frac{1}{2}\chi.C_L^{-1}.\chi}, \quad (60)$$

we are led to introduce the action

$$\mathcal{S}[\chi,\lambda_1,\lambda_2] = \lambda_1\left(\delta_{L1}-\delta_{Lq1}[\chi]\right)+\lambda_2\left(\delta_{L2}-\delta_{Lq2}[\chi]\right) +\frac{1}{2}\,\chi.C_L^{-1}.\chi \quad (61)$$

which now involves the two Lagrange multipliers λ_1 and λ_2. We again obtain the minimizer of the Gaussian weight $\Gamma_{12}=(\chi.C_L^{-1}.\chi)/2$ of Eq.(60) by differentiating the action $\mathcal{S}$ with respect to χ, λ_1 and λ_2, and we solve these equations as a perturbative series over $f_{\rm NL}$. At order zero we recover the Gaussian terms

$$\chi^{(0)}(\mathbf{q}) = \lambda_1^{(0)}\int_{V_1}\frac{\mathrm{d}\mathbf{q}_1}{V_1}\,C_L(\mathbf{q},\mathbf{q}_1)+\lambda_2^{(0)}\int_{V_2}\frac{\mathrm{d}\mathbf{q}_2}{V_2}\,C_L(\mathbf{q},\mathbf{q}_2) \quad (62)$$

$$\lambda_1^{(0)} = \frac{\sigma_2^2\,\delta_{L1}-\sigma_{12}^2\,\delta_{L2}}{\sigma_1^2\,\sigma_2^2-\sigma_{12}^4}, \quad (63)$$

$$\lambda_2^{(0)} = \frac{\sigma_1^2\,\delta_{L2}-\sigma_{12}^2\,\delta_{L1}}{\sigma_1^2\,\sigma_2^2-\sigma_{12}^4}, \quad (64)$$

where we note $\sigma_i^2=\sigma^2_{q_i,q_i}(0)$ and $\sigma_{12}^2=\sigma^2_{q_1,q_2}(s)$ from Eq.(15). At first order we obtain

$$\chi^{(1)}(\mathbf{q}) = \lambda_1^{(1)}\int_{V_1}\frac{\mathrm{d}\mathbf{q}_1}{V_1}\,C_L(\mathbf{q},\mathbf{q}_1)+\lambda_2^{(1)}\int_{V_2}\frac{\mathrm{d}\mathbf{q}_2}{V_2}\,C_L(\mathbf{q},\mathbf{q}_2) +2\lambda_1^{(0)}\int_{V_1}\frac{\mathrm{d}\mathbf{q}_1}{V_1}\int\mathrm{d}\mathbf{q}_1'\mathrm{d}\mathbf{q}_2'\,f_{\rm NL}^{\delta}(\mathbf{q}_1;\mathbf{q}_1',\mathbf{q}_2')\,C_L(\mathbf{q},\mathbf{q}_1')\,\chi^{(0)}(\mathbf{q}_2') +2\lambda_2^{(0)}\int_{V_2}\frac{\mathrm{d}\mathbf{q}_2}{V_2}\int\mathrm{d}\mathbf{q}_1'\mathrm{d}\mathbf{q}_2'\,f_{\rm NL}^{\delta}(\mathbf{q}_2;\mathbf{q}_1',\mathbf{q}_2')\,C_L(\mathbf{q},\mathbf{q}_1')\,\chi^{(0)}(\mathbf{q}_2') \quad (65)$$

$$\lambda_1^{(1)}(\sigma_1^2\sigma_2^2-\sigma_{12}^4) = \lambda_1^{(0)2}\left[\sigma_{12}^2(2f_{1;12}+f_{2;11})-3\sigma_2^2 f_{1;11}\right] +2\lambda_1^{(0)}\lambda_2^{(0)}\left[\sigma_{12}^2(2f_{2;12}+f_{1;22})-\sigma_2^2(2f_{1;12}+f_{2;11})\right] +\lambda_2^{(0)2}\left[3\sigma_{12}^2 f_{2;22}-\sigma_2^2(2f_{2;12}+f_{1;22})\right], \quad (66)$$

and

$$\lambda_2^{(1)}(\sigma_1^2\sigma_2^2-\sigma_{12}^4) = \lambda_1^{(0)2}\left[3\sigma_{12}^2 f_{1;11}-\sigma_1^2(2f_{1;12}+f_{2;11})\right] +2\lambda_1^{(0)}\lambda_2^{(0)}\left[\sigma_{12}^2(2f_{1;12}+f_{2;11})-\sigma_1^2(2f_{2;12}+f_{1;22})\right] +\lambda_2^{(0)2}\left[\sigma_{12}^2(2f_{2;12}+f_{1;22})-3\sigma_1^2 f_{2;22}\right], \quad (67)$$

where we note for instance $f_{1;22}=f_{a;bb}(s)$ and $f_{2;12}=f_{b;ab}(s)$, with $V_a=V_1$, $V_b=V_2$, from Eqs.(19)-(20). Next, the Gaussian weight $\Gamma_{12}=(\chi.C_L^{-1}.\chi)/2$ reads at order zero

$$\Gamma_{12}^{(0)} = \frac{\sigma_2^2\,\delta_{L1}^2+\sigma_1^2\,\delta_{L2}^2-2\sigma_{12}^2\,\delta_{L1}\delta_{L2}}{2\,(\sigma_1^2\,\sigma_2^2-\sigma_{12}^4)}, \quad (68)$$

and at first order,

$$\Gamma_{12}^{(1)} = \lambda_1^{(1)}\left(\sigma_1^2\lambda_1^{(0)}+\sigma_{12}^2\lambda_2^{(0)}\right)+\lambda_2^{(1)}\left(\sigma_{12}^2\lambda_1^{(0)}+\sigma_2^2\lambda_2^{(0)}\right) +2\lambda_1^{(0)3}f_{1;11}+2\lambda_1^{(0)2}\lambda_2^{(0)}(2f_{1;12}+f_{2;11}) +2\lambda_1^{(0)}\lambda_2^{(0)2}(2f_{2;12}+f_{1;22})+2\lambda_2^{(0)3}f_{2;22}. \quad (69)$$

Therefore, in the rare-event limit the tail of the bivariate distribution (60) reads as

$$\mathcal{P}_L(\delta_{L1},\delta_{L2}) \sim \mathcal{P}_L(\delta_{L1})\,\mathcal{P}_L(\delta_{L2})\,e^{-\Delta\Gamma}, \quad (70)$$

with

$$\Delta\Gamma = \Gamma_{12}-\Gamma_1-\Gamma_2, \quad (71)$$

where Γ_{12} is given by Eqs.(68)-(69), and Γ_1 and Γ_2 by Eqs.(42)-(43) for each sphere V_1 and V_2. Next, following Valageas (2009b), we write the halo two-point correlation as

$$1+\xi_{M_1,M_2}(x) = (1+\delta_{LM}(s))\,e^{-\Delta\Gamma}, \quad (72)$$

where the factor $(1+\delta_{LM}(s))$ models the effects associated with the mapping from Lagrangian to Eulerian space. This is the local linear density contrast at radius s from a halo of mass $M=\max(M_1,M_2)$ (to keep the symmetry $M_1\leftrightarrow M_2$), as given by Eqs.(39)-(40). A sufficiently accurate approximation would be to use only the zeroth-order term (39), as shown by Fig. 1, but taking into account the correction (40) brings no further difficulty. Here we approximated the nonlinear density contrast δ_M by the linear density contrast δ_{LM}, since at large distance where $\delta_M\ll 1$ we have $\delta_M\simeq\delta_{LM}$. Next, we must express the Lagrangian separation s in terms of the Eulerian distance x. Following Valageas (2009b), at lowest order where we consider each halo as a test particle that falls into the potential well built by the other halo, we obtain s as the solution of the implicit equation

$$x = s\left(1-\frac{\delta_{LM_1}(s)}{3}-\frac{\delta_{LM_2}(s)}{3}\right), \quad (73)$$

where $\delta_{LM_i}(s)$ is the linear density contrast within radius s of the halo of mass M_i, given by Eqs.(36)-(37). At large separation, this relation can be inverted as

$$s = x\left(1+\frac{\delta_{LM_1}(x)}{3}+\frac{\delta_{LM_2}(x)}{3}\right), \quad (74)$$

which provides an explicit expression for s.

Finally, we define the real-space halo bias as the ratio of the halo and matter two-point correlations,

$$b^2_{M_1,M_2}(x) = \frac{\xi_{M_1,M_2}(x)}{\xi(x)}. \quad (75)$$

Since at large distance the matter correlation is within the linear regime, $\xi(x)\simeq\sigma^2_{0,0}(x)$, we also write in this limit

$$b^2_{M_1,M_2}(x) \simeq \frac{\xi_{M_1,M_2}(x)}{\sigma^2_{0,0}(x)}, \quad (76)$$

which fully determines the halo bias from Eq.(72).

For equal-mass halos of radius q, defined by the same threshold δ_L, the two Lagrange multipliers are equal, $\lambda_1=\lambda_2=\lambda$, and Eqs.(63)-(64), (66)-(67), simplify as

$$\lambda^{(0)} = \frac{\delta_L}{\sigma^2+\sigma_{12}^2}, \quad (77)$$

and

$$\lambda^{(1)} = \frac{-3\,\delta_L^2}{(\sigma^2+\sigma_{12}^2)^3}\,(f_{2;11}+2f_{1;12}+f_{1;11}), \quad (78)$$

where we note $\sigma^2 = \sigma_q^2$. This yields for the Gaussian weight Γ_{12},

$$\Gamma_{12}^{(0)} = \frac{\delta_L^2}{\sigma^2+\sigma_{12}^2}, \quad (79)$$

and

$$\Gamma_{12}^{(1)} = \frac{-2\,\delta_L^3}{(\sigma^2+\sigma_{12}^2)^3}\,(f_{2;11}+2f_{1;12}+f_{1;11}). \quad (80)$$

Then, the difference $\Delta\Gamma$ defined in Eq.(71), that measures the correlation between rare events in the linear density field, writes as

$$\Delta\Gamma^{(0)} = \frac{-\sigma_{12}^2\,\delta_L^2}{\sigma^2\,(\sigma^2+\sigma_{12}^2)}, \quad (81)$$

and

$$\Delta\Gamma^{(1)} = \frac{-2\,\delta_L^3}{(\sigma^2+\sigma_{12}^2)^3}\left[f_{2;11}+2f_{1;12}+\frac{\sigma^6-(\sigma^2+\sigma_{12}^2)^3}{\sigma^6}f_{1;11}\right] \quad (82)$$

We can check that $\Delta\Gamma$ vanishes for $s\to\infty$, since all mixed quantities, σ_{12}^2, $f_{1;12}$ and $f_{2;11}$, go to zero.

As stressed in Politzer & Wise (1984), real-space formulae such as (72), which are obtained in the rare-event ($\delta_L/\sigma \gg 1$) and large separation ($\sigma_{12} \ll \sigma$) limits, do not assume that the exponent $\Delta\Gamma$ is small. In fact, as shown in Valageas (2009b), at large redshift one can probe a regime where this exponent is large, so that one needs to keep the nonlinear form (72), which yields a nonlinear bias. As seen from Eq.(81), this regime corresponds to very massive halos, $\delta_L/\sigma\to\infty$, at fixed (small) ratio σ_{12}/σ. Nevertheless, in the regime where $\Delta\Gamma$ is small (i.e. in the large separation limit $x\to\infty$), which covers the cases of interest encountered at low redshift, we can expand the exponential in Eq.(72). Then, at lowest order over the terms that vanish in the large separation limit, we obtain for equal-mass halos

$$x\to\infty: \quad \xi_M(x) \simeq \delta_{LM}(s) - \Delta\Gamma, \quad (83)$$

whence

$$\xi_M(x) \simeq \frac{\delta_L}{\sigma_q^2}\,\sigma_{q,0}^2(s) + \frac{\delta_L^2}{\sigma_q^4}\left[f_{0;qq}(s)+2f_{q;0q}(s)-3\frac{f_{q;qq}}{\sigma_q^2}\sigma_{q,0}^2(s)\right] + \frac{\delta_L^2}{\sigma_q^4}\sigma_{q,q}^2(s) + 2\frac{\delta_L^3}{\sigma_q^6}\left[f_{2;11}(s)+2f_{1;12}(s)-3\frac{f_{1;11}}{\sigma_q^2}\sigma_{q,q}^2(s)\right] \quad (84)$$

Hereafter we call the bias $b_M^2(x)$ obtained from Eq.(84) and Eq.(76) as the "linearized" bias.

We can note that, following the approach of Kaiser (1984), Matarrese & Verde (2008) also computed the effect of local-type non-Gaussianity (1) on the halo two-point correlation. Drawing on earlier work by Matarrese et al. (1986), who compute the n-point halo correlations by expanding the relevant path-integrals and next resumming the series within a large-distance and rare-event approximation, they obtain expressions of the form (72), without the prefactor $(1+\delta_{LM})$, and (84), without the terms in the first line, that arise from this prefactor, and the last term $f_{1;11}$ in the second bracket. This latter term arises from the factor σ_{12}^2 in the denominator of expression (80), associated with the effect of primordial non-Gaussianity on the one-point distribution (43). It can be seen as a renormalization of the Gaussian term $(\delta_L^2/\sigma_q^4)\sigma_{q,q}^2(s)$, since it shows the same scale dependence through the function $\sigma_{q,q}^2(s)$. The presence of such a term was already noticed in Slosar et al. (2008) in Fourier space, and Desjacques et al. (2009) pointed out that it needs to be included to obtain a good agreement with numerical simulations. This will give rise to the last term in Eq.(85) and the second term in Eqs.(91) and (93) below. On the other hand, the terms in the first line of Eq.(84), associated with the prefactor $(1+\delta_{LM})$ in Eq.(72), are due to the mapping from Lagrangian to Eulerian space, and the first bracket in Eq.(84) expresses the (small) effect of primordial non-Gaussianity on this mapping. Another difference between Eqs.(72) and (84) and previous works is that (within some approximation) we take into account the difference between Lagrangian and Eulerian distances s and x. This can play a non-negligible role as seen in Fig. 5 below.

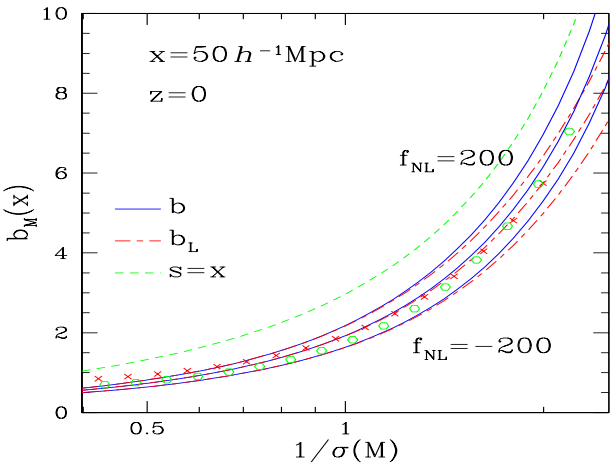

Fig. 5. The halo bias $b_M(x)$, as a function of $\sigma(M)$, at fixed redshift $z=0$ and distance $x=50h^{-1}$Mpc. The solid lines "b" are the nonlinear theoretical prediction of Eqs.(72), (73) and (76), for $f_{\rm NL}=\pm200$ and $f_{\rm NL}=0$ (i.e. Gaussian case, intermediate line), while the dot-dashed lines "b_L" are the linearized bias of Eq.(84). The upper dashed line "$s=x$" shows the result obtained in the Gaussian case by setting $s=x$ in Eq.(72). The points are the fits to Gaussian numerical simulations, from Sheth, Mo & Tormen (2001) (crosses) and Pillepich (2009) (circles).

We show in Fig. 5 the halo bias $b_M(x)$, as a function of $\sigma(M)$ at fixed distance $x=50h^{-1}$ Mpc and redshift $z=0$, for $f_{\rm NL}=\pm200$ and $f_{\rm NL}=0$. We display both the nonlinear result (solid line) of Eq.(72) and the linear result (dot-dashed line) of Eq.(84). In addition, for the Gaussian case we also display the bias obtained by setting $s=x$ in Eq.(72). As in Valageas (2009b), for the Gaussian case ($f_{\rm NL}=0$) we obtain a good agreement with the fits to numerical simulations of Sheth, Mo & Tormen (2001) and Pillepich (2009). Moreover, we can see that it is important to take into account the displacement of the halos through

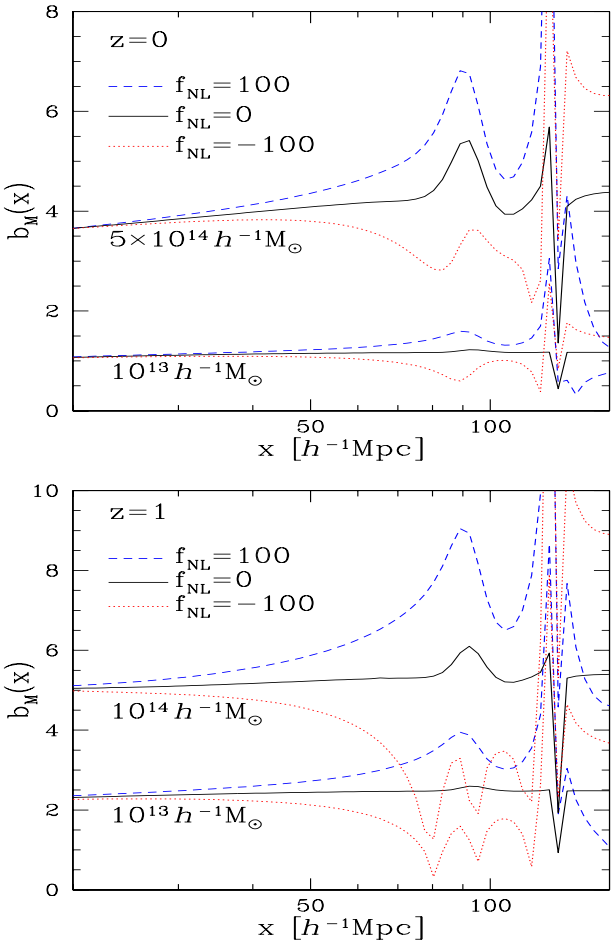

Fig. 6. The halo bias $b_M(x)$ as a function of distance x, at redshifts $z = 0$ (upper panel) and $z = 1$ (lower panel), for several masses. We show the cases $f_{\rm NL} = 0$ (solid lines), $f_{\rm NL} = 100$ (dashed lines) and $f_{\rm NL} = -100$ (dotted lines). The divergences at $x \sim 120h^{-1}$Mpc are due to the fact that the halo and matter correlations do not change sign at the same distance.

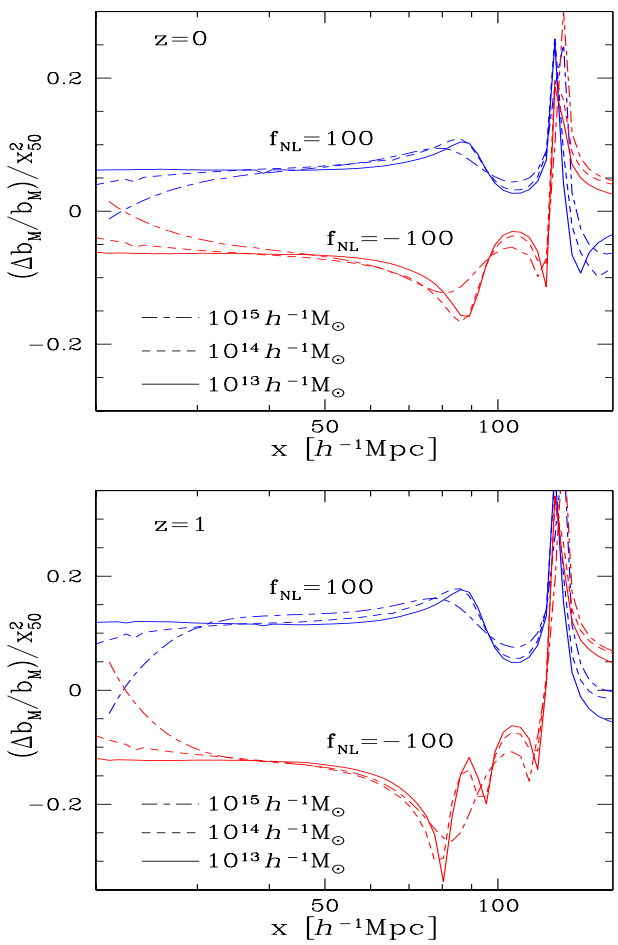

Fig. 7. The real-space ratio $[\Delta b_M(x, f_{\rm NL})/b_M(x, 0)]/x_{50}^2$ of the correction $\Delta b_M(x, f_{\rm NL}) = b_M(x, f_{\rm NL}) - b_M(x, 0)$ to the Gaussian bias $b_M(x, 0)$, divided by the factor x_{50}^2 with $x_{50} = x/(50h^{-1}{\rm Mpc})$, as a function of distance x. We show the cases $f_{\rm NL} = 100$ (upper lines) and $f_{\rm NL} = -100$ (lower lines) for several masses at redshifts $z = 0$ (upper panel) and $z = 1$ (lower panel), from Eq.(72). Larger masses have a steeper slope at low x.

Eq.(73), as the approximation $s = x$ significantly overestimates the bias. We checked that using the simpler Eq.(74) gives a close result to the one obtained with Eq.(73) and also agrees with the simulations. Thus, for practical purposes it is sufficient to use Eq.(74). We can see that for all cases shown in Fig. 5 the linear bias from Eq.(84) gives results that are very close to the fully nonlinear expression (72). This justifies the use of such linearized expressions in this regime. This will be especially useful in section 4.2, where we consider the bias of dark matter halos in Fourier space. Indeed, it is easier to take the Fourier transform of Eq.(84), which allows to recover the results obtained in previous works. Thus, one interest of the real-space results (72)-(84) is to provide a check on whether linearized predictions (i.e. where the halo correlation only involves the matter power spectrum at linear order) are valid. Then, in agreement with those studies (that were mostly performed in Fourier space and led to Eq.(2), see Dalal et al. 2008; Slosar et al. 2008), and with Eq.(84), we can see that the deviation from the Gaussian bias, $b_M(x, f_{\rm NL}) - b_M(x, 0)$, grows linearly with $b_M(x, 0)$ at large bias and has the same sign as $f_{\rm NL}$.

Next, we display in Fig. 6 the dependence on the distance x of the bias obtained for several masses at redshifts $z = 0$ and $z = 1$. More precisely, we show the ratio $\sqrt{|\xi_M(x)/\xi(x)|}$, since the halo and matter correlations do not change sign at the same point. We plot the cases $f_{\rm NL} = \pm 100$ as well as the Gaussian case $f_{\rm NL} = 0$. While the Gaussian bias is roughly constant over large scales, up to $\sim 100h^{-1}$Mpc, in agreement with previous studies (e.g., Mo & White 1996; Mo et al. 1997), the non-Gaussian bias shows a strong scale dependence, with a deviation from the Gaussian bias that roughly grows as x^2 up to $\sim 100h^{-1}$Mpc. This agrees with the k^{-2} behavior observed in Fourier space, see Eq.(2) above (Dalal et al. 2008; Slosar et al. 2008) and Eq.(93) below.

In order to see more clearly the scaling of the real-space correction $\Delta b_M(x, f_{\rm NL}) = b_M(x, f_{\rm NL}) - b_M(x, 0)$ to the Gaussian bias, we show in Fig. 7 the ratio $[\Delta b_M(x, f_{\rm NL})/b_M(x, 0)]/x_{50}^2$, with $x_{50} = x/(50h^{-1}{\rm Mpc})$.

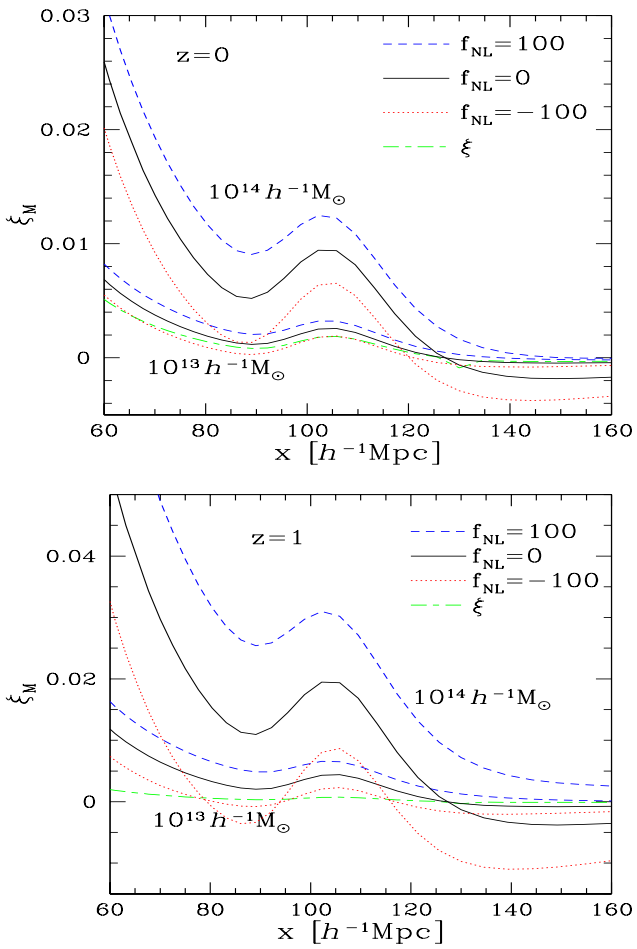

Fig. 8. The halo ($f_{\rm NL}=0,\pm100$) and matter (ξ) two-point correlations at redshifts $z=0$ (upper panel) and $z=1$ (lower panel). We show the curves obtained for the masses $M=10^{13}$ and $10^{14}h^{-1}M_\odot$.

We display the results obtained from Eq.(72) for several masses at $z=0$ (upper panel) and $z=1$ (lower panel), for $f_{\rm NL}=\pm100$. We can see that over the range $30<x<90h^{-1}$Mpc all curves roughly collapse onto one another. This means that over this range the real-space correction roughly scales as $\Delta b_M(x)\propto f_{\rm NL}b_M(x,0)x^2$, which roughly agrees with the Fourier-space scaling (2) (here we neglected any constant offset, such as the factor -1 in Eq.(2), see the discussion of Eq.(94) below). In fact, it appears that our predictions scale more closely as x^2, as shown in Fig. 7, than as $\alpha(1/x)^{-1}$, that would be suggested by Eqs.(2), (93) (at these scales the transfer function already deviates from unity). This agrees with the behavior observed in Fourier space in Fig. 11 below. Note that the masses shown in Fig. 7 span the range $1.2<b_M(x,0)<5.9$ at $x=50h^{-1}$Mpc and $z=0$, and $2.4<b_M(x,0)<15.4$ at $z=1$, so that the linear scaling with $b_M(x,0)$ of the correction $\Delta b_M(x,f_{\rm NL})$ appears to be a good approximation.

Below $30h^{-1}$Mpc large masses show a steeper scale dependence for $\Delta b_M(x,f_{\rm NL})$. At very large distance, $x>100h^{-1}$Mpc, the oscillations seen in Figs. 6 and 7 are due to the baryon acoustic oscillation. Indeed, since the halo correlation is not exactly proportional to $\sigma^2_{0,0}(x)$, even in the Gaussian case and in the linear regime (for instance it involves the smoothing scale q, see Eq.(84)), the baryon oscillations seen in the halo and matter two-point correlations are not exactly proportional. This yields the non-monotonic behavior seen in Figs. 6 and 7 around $100h^{-1}$Mpc. For the same reason, the halo and matter correlations do not exactly vanish at the same distance, which gives rise to the divergent spike at $\sim 120h^{-1}$ Mpc. These features simply mean that at these scales it is no longer useful to work with the bias b_M, which only makes sense if the halo and matter correlations are roughly proportional. In this range, where the correlations show some oscillations and change sign it is no longer a good approximation to write the halo correlation in terms of the matter correlation multiplied by some slowly varying bias factor. Then, one rather needs to directly study the halo and matter correlations themselves.

Thus, we compare in Fig. 8 the halo and matter two-point correlations. We focus on large scales to see how the baryon acoustic oscillation is modified when one uses massive halos as a tracer of the initial matter power spectrum. In agreement with previous works (Desjacques 2008) we can see that the oscillation is strongly amplified for massive halos that have a large bias. This amplification still holds for significant primordial non-Gaussianity ($f_{\rm NL}=\pm100$), although it appears to be slightly lower for positive $f_{\rm NL}$. Moreover, the peak of the oscillation shows no significant shift, so that a measure of its position appears to be a robust ruler to constrain cosmology, independently of the halo bias and of the primordial non-Gaussianity. By contrast, we can note that the distance at which the two-point correlation changes sign is not significantly modified as one goes from the matter to the halo correlation in the Gaussian case, but it is rather sensitive to the primordial non-Gaussianity. In particular, a positive $f_{\rm NL}$ shifts this point to a larger distance. However, theoretical and observational error bars may be too large to use this effect to constrain $f_{\rm NL}$ in a competitive manner as compared with other probes.

4.2. Fourier-space bias

Rather than the real-space two-point correlation, recent works have mostly studied the effect of primordial non-Gaussianity on the halo power spectrum, where at lowest order the Poisson equation (3) directly gives an estimate of the form (2) for the deviation from the bias obtained with Gaussian initial conditions (Dalal et al. 2008; Slosar et al. 2008).

It is not convenient to take the Fourier transform of the nonlinear correlation (72), but at moderate redshifts we have seen that the linearized form (84) provides a very good approximation. Then, if we also make the approximation $s\simeq x$, which is valid at lowest order, the Fourier transform of Eq.(84) readily gives the halo power spectrum as

$$P_M(k) \simeq \frac{\delta_L}{\sigma_q^2}P_L(k)\tilde{W}(kq)+\frac{\delta_L^2}{\sigma_q^4}\left[\tilde{f}_{0;qq}(k)+2\tilde{f}_{q;0q}(k) -3\frac{f_{q;qq}}{\sigma_q^2}P_L(k)\tilde{W}(kq)\right]+\frac{\delta_L^2}{\sigma_q^4}P_L(k)\tilde{W}(kq)^2 +2\frac{\delta_L^3}{\sigma_q^6}\left[\tilde{f}_{2;11}(k)+2\tilde{f}_{1;12}(k)-3\frac{f_{1;11}}{\sigma_q^2}P_L(k)\tilde{W}(kq)^2\right], \quad (85)$$

where the quantities $\tilde{f}$ are obtained from Eqs.(21)-(22). As discussed below Eq.(84), the terms $\tilde{f}_{2;11}(k)$ and $2\tilde{f}_{1;12}(k)$

in Eq.(85) were already obtained by Matarrese & Verde (2008), following also Kaiser (1984) by identifying massive halos with rare fluctuations in the linear density field. Defining the Fourier-space bias as (note that this is not the Fourier transform of the real-space bias (75))

$$b_M^2(k) = \frac{P_M(k)}{P(k)} \simeq \frac{P_M(k)}{P_L(k)}, \tag{86}$$

where we used $P(k) \simeq P_L(k)$ at low k for the matter power spectrum, we obtain $b_M^2(k)$ from Eq.(85). We can also obtain the bias of different-mass halos in a similar fashion, first expanding Eq.(72) and next taking the Fourier transform. In order to take into account the displacement of the halos (i.e. $x \neq s$), we can also make the approximation

$$P_M(k) \to \left(\frac{x}{s}\right)^3 P_M\left(\frac{x}{s}k\right), \quad \text{with} \quad x = \frac{1}{k}, \tag{87}$$

where we use the explicit expression (74) for $s(x)$. This expresses the fact that because of the displacement of massive halos, which usually have come closer because of their mutual attraction ($x < s$), Lagrangian-space wavelengths $\sim s$ (i.e. measured in the linear density field) correspond to smaller Eulerian-space wavelengths $\sim x$ (i.e. measured in the nonlinear density field). This also follows the spirit of the Hamilton et al. (1991) ansatz, translated in Fourier space in Peacock & Dodds (1996).

We can note that for large negative $f_{\rm NL}$ the halo power spectrum (85) can become negative. This is due to the fact that we looked for an expression of the halo correlation, or of the halo power spectrum, at linear order over $f_{\rm NL}$ as in Eq.(85). However, by definition the power spectrum $P_M(k)$ must be positive. Then, in cases where the expression (85) turns negative one should consider higher-order terms over $f_{\rm NL}$, which would ensure that the power spectrum remains positive. Nevertheless, since such high-order terms are beyond the scope of this article, we consider below the following simple procedure that ensures that $P_M(k)$, or the squared bias $b_M^2(k)$, remain positive. Up to linear order over $f_{\rm NL}$, the bias (86) reads as

$$b_M(k,f_{\rm NL}) = \sqrt{\frac{P_M(k,0)+\Delta P_M(k,f_{\rm NL})}{P(k)}} \simeq b_M(k,0)\left(1+\frac{1}{2}\frac{\Delta P_M(k,f_{\rm NL})}{P_M(k,0)}\right), \tag{88}$$

where $\Delta P_M(k,f_{\rm NL}) = P_M(k,f_{\rm NL}) - P_M(k,0)$ is the deviation from the Gaussian halo power spectrum and we expanded the square-root. Then, we may use the last expression (88) as the prediction for the halo bias. This amounts to make the transformation

$$b_M^2(k,f_{\rm NL}) \to b_M^2(k,0)\left[1+\frac{1}{2}\left(\frac{b_M^2(k,f_{\rm NL})}{b_M^2(k,0)}-1\right)\right]^2, \tag{89}$$

where the two sides only differ by higher-order terms over $f_{\rm NL}$ (as $1+\epsilon \simeq (1+\epsilon/2)^2$ up to linear order over ϵ) and the right side is always positive.

If we take the limit of very rare events, that is $\sigma_q \to 0$ in Eq.(85), we can only keep the last two terms (note that $\tilde{f} \propto \sigma_q^2$, see Eq.(92) below),

$$\sigma_q \to 0: \quad P_M(k) \sim P_L(k)\tilde{W}(kq)^2\left[\frac{\delta_L^2}{\sigma_q^4} - 6\frac{\delta_L^3\, f_{1;11}}{\sigma_q^8}\right]$$

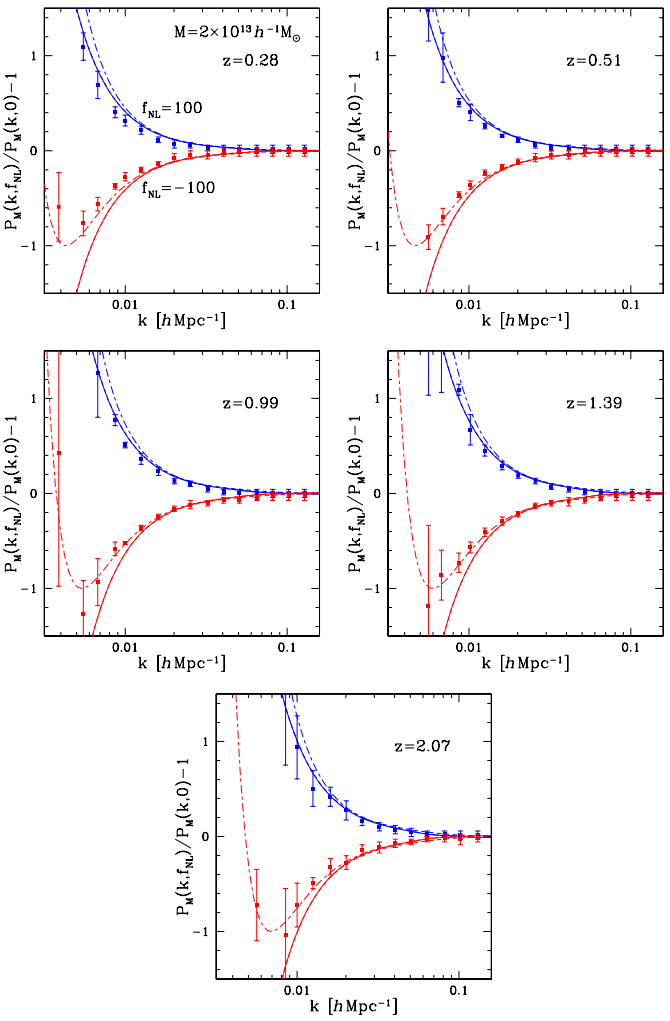

Fig. 9. The correction to the halo power spectrum due to primordial non-Gaussianity. We show the ratio $P_M(k,f_{\rm NL})/P_M(k,0)-1$ for $f_{\rm NL}=100$ (upper curves) and $f_{\rm NL}=-100$ (lower curves). The solid and dashed curves that are almost indistinguishable are Eqs.(85) and (87). The dot-dashed curves, that are above the solid curves at low k, correspond to Eq.(89) which ensures that the halo power spectrum is always positive. The theoretical predictions are for $M = 2\times10^{13}h^{-1}M_\odot$ and the data points are the numerical simulations of Desjacques et al. (2009), for $M > 2\times10^{13}h^{-1}M_\odot$.

$$+2\frac{\delta_L^3}{\sigma_q^6}\left(\tilde{f}_{2;11}(k)+2\tilde{f}_{1;12}(k)\right). \tag{90}$$

At low k, with $\tilde{W}(kq) \simeq 1$, and at linear order over $f_{\rm NL}$, the square root of Eq.(86) gives with Eq.(90) the bias

$$\sigma_q \to 0, \quad k \to 0: \quad b_M(k) \sim \frac{\delta_L}{\sigma_q^2} - 3\frac{\delta_L^2}{\sigma_q^6}f_{1;11} + \frac{\delta_L^2}{\sigma_q^4}\frac{\tilde{f}_{2;11}(k)+2\tilde{f}_{1;12}(k)}{P_L(k)}. \tag{91}$$

The first term, δ_L/σ_q^2, is the result obtained by Kaiser (1984) for rare massive halos (i.e. with a large bias) for Gaussian initial conditions. It is interesting to note that

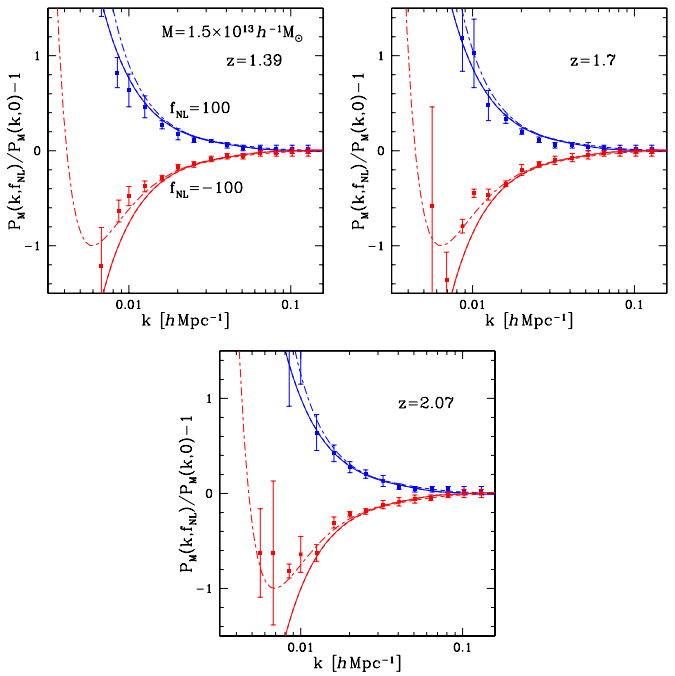

Fig. 10. Same as Fig. 9, but for $M = 1.5\times10^{13}h^{-1}M_\odot$. The data points are the numerical simulations of Desjacques et al. (2009), for $10^{13} < M < 2\times10^{13}h^{-1}M_\odot$.

the second term gives a scale-independent correction to the Gaussian bias. The presence of such a term was already noticed in Slosar et al. (2008) and Afshordi & Tolley (2009). As stressed in Desjacques et al. (2009), taking this term into account is required to obtain a good match to numerical simulations. We checked that this is indeed the case to match the numerical results in Figs. 9 and 10 below using Eq.(85). The last two terms depend on the wavenumber k. There is an additional term, that we neglect in this paper, that arises from the dependence of the matter power spectrum on $f_{\rm NL}$ (i.e. the denominator in Eq.(86)). However, since this term is much smaller than the other ones we disregard it here (see Desjacques et al. 2009). For the local non-Gaussianity (7), we have from Eqs.(21)-(22),

$$k\to 0: \quad \tilde{f}_{2;11}(k) \sim f_{\rm NL}\,\alpha(k)\int {\rm d}\mathbf{k}_1\, P_L(k_1)^2\,\frac{\tilde{W}(k_1 q)^2}{\alpha(k_1)^2},$$
$$\tilde{f}_{1;12}(k) \sim f_{\rm NL}\,\frac{\sigma_q^2\,P_L(k)}{\alpha(k)}, \qquad (92)$$

which yields from Eq.(91)

$$\sigma_q\to 0,\ \ k\to 0: \quad b_M(k)\sim \frac{\delta_L}{\sigma_q^2}-3\frac{\delta_L^2}{\sigma_q^6}f_{1;11}+f_{\rm NL}\frac{2\delta_L^2}{\sigma_q^2\alpha(k)}. \qquad (93)$$

Thus, we recover the k^{-2} dependence at low k brought by the local-type non-Gaussianity (1), through the $1/\alpha(k)$ factor in the last term. The second term in Eq.(93) is the constant shift due to the non-Gaussianity noticed above.

We compare in Figs. 9 and 10 our results for the Fourier-space bias $b_M^2(k)$ with numerical simulations from Desjacques et al. (2009). Since the dependence on mass is rather weak, we show in Fig. 9 our results for $M = 2\times10^{13}h^{-1}M_\odot$, whereas the data points are for $M > 2\times10^{13}h^{-1}M_\odot$, and we show in Fig. 10 our results for $M = 1.5\times10^{13}h^{-1}M_\odot$, whereas the data points are for $10^{13} < M < 2\times10^{13}h^{-1}M_\odot$. The predictions (85) (solid lines) and (87) (dashed lines) are almost indistinguishable in this regime and agree reasonably well with the simulations, except at low k for $f_{\rm NL} = -100$ where they give a negative halo power spectrum. The dot-dashed line, which corresponds to Eq.(89), gives a much better fit to simulations at low k for negative $f_{\rm NL}$, as could be expected from the fact that it always gives a positive halo power spectrum. However, a priori one should not give too much weight to this improved accuracy in this regime. Indeed, as is clear from Eqs.(88)-(89), the solid and dot-dashed curves in Figs. 9-10 only differ by terms of order $f_{\rm NL}^2$ and beyond. Since all our results have been derived at linear order over $f_{\rm NL}$ one can expect that Eq.(89) does not include all terms of order $f_{\rm NL}^2$. Then, although for practical purposes it is better to use Eq.(89) in this regime (i.e. negative $f_{\rm NL}$ at low k) it is still useful to also consider Eq.(85), as the deviation between both predictions should give an estimate of the theoretical uncertainty. Let us point out here that, in contrast with some previous approaches (e.g., Grossi et al. 2009; Desjacques et al. 2009), the good agreement with numerical simulations shown in Figs. 9 and 10 is obtained from Eq.(85) without any fitting parameter (such as the rescaling parameter q in Grossi et al. (2009) or the mass function parameters in Desjacques et al. (2009)).

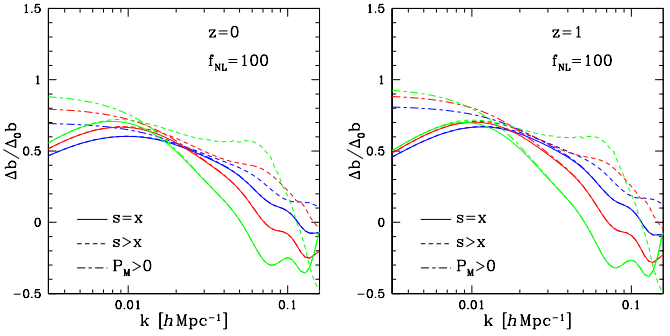

Fig. 11. The Fourier-space ratio $\Delta b_M(k,f_{\rm NL})/\Delta_0 b_M(k,f_{\rm NL})$ of the correction $\Delta b_M(k,f_{\rm NL}) = b_M(k,f_{\rm NL}) - b_M(k,0)$ to the Gaussian bias $b_M(k,0)$, divided by the scaling factor $\Delta_0 b_M$ defined in Eq.(94), as a function of wavenumber k. We show the case $f_{\rm NL} = 100$ for several masses, $M = 10^{13}$ (blue), 10^{14} (red) and $10^{15}h^{-1}M_\odot$ (green), at redshifts $z = 0$ (left panel) and $z = 1$ (right panel). The curves labelled "$s = x$", "$s > x$" and "$P_M > 0$" correspond to Eqs.(85), (87) and (89) respectively.

As in Fig. 7, in order to see more clearly the scaling of the correction $\Delta b_M(k,f_{\rm NL}) = b_M(k,f_{\rm NL}) - b_M(k,0)$ to the Fourier-space Gaussian bias, we show in Fig. 11 the ratio $\Delta b_M(k,f_{\rm NL})/\Delta_0 b_M(k,f_{\rm NL})$, where we now define

$$\Delta_0 b_M(k,f_{\rm NL}) = f_{\rm NL}\,b_M(k,0)\,\frac{2\delta_L}{\alpha(k)}. \qquad (94)$$

The correction obtained from a simple peak-background split argument rather gives $\Delta b_M(k,f_{\rm NL}) = f_{\rm NL}[b_M(k,0) - 1](2\delta_L/\alpha(k))$, as in Eq.(2), see Dalal et al. (2008); Slosar

et al. (2008). However, in our formalism both the leading term δ_L^2/σ_q^4 (third term in Eq.(85)) and the subleading term δ_L/σ_q^2 (first term in Eq.(85)) are modified by primordial non-Gaussianity (the terms in the brackets that follow). The term δ_L/σ_q^2 arises from the Lagrangian to Eulerian space mapping (the prefactor $(1+\delta_{LM})$ in Eq.(72)) and it corresponds to the factor 1 in the more usual Eq.(2), that is not modified in the simplest model. However, in general we can expect non-Gaussianities to also affect this Lagrangian to Eulerian space mapping, and our model gives an estimate of this effect through Eq.(40). Therefore, we scale $\Delta_0 b_M(k, f_{\rm NL})$ with $b_M(k,0)$ rather than with $[b_M(k,0)-1]$ in Eq.(94). We show in Fig. 7 the results obtained at redshifts $z=0$ and $z=1$ for several masses. The curves labelled "$s=x$", "$s>x$" and "$P_M>0$" correspond to Eqs.(85), (87) and (89) respectively. We can see that the collapse of the curves obtained for different masses is not exact, as could be expected since Eq.(85) is more complex than Eq.(94), but the scaling (94) still captures most of the dependence on the halo mass M. In fact, most of the dispersion seen in Fig. 7 does not arise from the different masses but from the various approximations (85), (87) and (89). This should provide an estimate of the theoretical uncertainty. As in Figs. 9 and 10, Eq.(89), which involves higher-order terms over $f_{\rm NL}$ to ensure that $P_M(k)$ is always positive, rises above Eq.(85) at low k ($k<0.01h$ Mpc^{-1}) and is indistinguishable at higher k, whereas Eq.(87) rises above (85) at high k ($k>0.01h$ Mpc^{-1}), where the correction $\Delta b_M(k, f_{\rm NL})$ is quite small, and is indistinguishable at lower k. Approximations (89) and (87) are likely to be most accurate at low and high k respectively, see also Figs. 9 and 10. In any case, we can see that the scaling with wavenumber, $\Delta b_M(k, f_{\rm NL}) \sim 1/\alpha(k)$, is slightly broken, although this still provides a good approximation. In agreement with the numerical simulations of Desjacques et al. (2009), we can see that the ratio $\Delta b/\Delta_0 b$ is suppressed at high k, which means that the correction $\Delta b_M(k, f_{\rm NL})$ decreases slightly faster than $1/\alpha(k)$ over the range $0.01-0.1h$ Mpc^{-1}. In fact, in agreement with the real-space behavior seen in Fig. 7, it appears that over this range the correction $\Delta b_M(k, f_{\rm NL})$ scales slightly more closely as k^{-2} than as $1/\alpha(k)$, although none of these two behaviors is exact.

5. Conclusion

We have shown in this article how to extend to non-Gaussian initial conditions the computation of the mass function and of the bias of dark matter halos presented in Valageas (2009b) for the Gaussian case. This relies on a saddle-point approach, that allows to derive the large-mass asymptotic tails of the quantities of interest from the statistical weight of the initial conditions, supplemented by additional nonlinear constraints. Then, focussing on the case of "$f_{\rm NL}$-type" primordial non-Gaussianity, where the linear gravitational potential can be written as the sum of linear and quadratic terms over an auxiliary Gaussian field χ, we explained how to obtain the relevant saddle-points as a perturbative series over the nonlinear parameter $f_{\rm NL}$. This method is very general and it applies to any case of small primordial non-Gaussianity, where Bardeen's potential (or equivalently, below the Hubble radius, the gravitational potential or the density field) can be written as a polynomial over a Gaussian field χ as

$$\Phi = \chi + \sum_{i=2}^{k} f_i \left(\chi^i - \langle \chi^i \rangle \right), \tag{95}$$

where the nonlinear parameters f_i are small. Then, following the method presented in sections 3, 4, the one-cell and two-cell saddle-points (associated with the one-point and two-point density distributions, whence the halo mass function and bias) can be computed as a perturbative series over the coefficients f_i (which need not be of the same order). This includes in particular the case of a cubic term $g_{\rm NL}\chi^3$. Of course, this also extends to the cases where the coefficients f_i are not mere numbers but convolution kernels and to several Gaussian fields χ_j (which can have a nonzero cross-correlation). In all such cases, the large-mass asymptotics are set by the statistical weight $e^{-(\chi_i.C_{ij}^{-1}.\chi_j)/2}$ of these Gaussian fields, taken at the saddle-point associated with the maximization of this weight under appropriate nonlinear constraints, that express the mapping from χ_j to the relevant quantity, such as the nonlinear density within a spherical cell.

Focussing on the case of local-type primordial non-Gaussianity, we described how to obtain, up to linear order over $f_{\rm NL}$, the one-cell saddle-point associated with the probability distributions $\mathcal{P}_L(\delta_L)$ and $\mathcal{P}(\delta)$ of the linear and nonlinear density contrasts within spherical cells. This gives the quasi-linear limit of these distributions as well as the large-mass exponential falloff of the halo mass function. An advantage of our method is that it allows us to explicitly check that realistic amounts of primordial non-Gaussianity have no significant effect on the density profile of this saddle-point. This ensures that shell-crossing appears for (almost) the same nonlinear density $\delta_+ \gtrsim 200$ (see Valageas 2009b), so that the large-mass tail of the halo mass function can be derived provided halos are defined by a nonlinear density threshold that is below this upper bound (which is indeed the case). Although this procedure only gives the large-mass tail, we have proposed a simple change of variable, applied to the mass function fitted to Gaussian numerical simulations, that obeys this large-mass asymptotic while keeping the mass function normalized to unity. If one uses the Press-Schechter mass function this gives back the result of Matarrese et al. (2000) but we argue that this procedure is somewhat more natural if one wishes to recover a more accurate mass function in the Gaussian case. We also checked that this agrees well with results from non-Gaussian numerical simulations.

Next, we applied this method to the two-point correlation of massive halos, following the approach of Kaiser (1984). As in Valageas (2009b) we take into account the displacement of halo pairs under their mutual gravitational attraction. This gives the real-space halo correlation $\xi_M(x)$, whence the real-space bias $b_M(x)$. Since this approach does not assume that the halo correlation is small, the nonlinear formula it yields can be used to check whether the "linearized" form (where one only keeps the linear term over the matter correlation $\xi(x)$) is a good approximation in the regime of interest. As expected, we find that the correction $\Delta b_M(x, f_{\rm NL})$ to the Gaussian bias grows with $b_M(x,0)$ and with scale, roughly as $f_{\rm NL} b_M(x,0) x^2$, up to $x \sim 100 h^{-1}$Mpc. Beyond this scale, the baryon acoustic oscillation and the fact that the halo and matter correlations

do not change sign at the same point lead to strong oscillations and divergent spikes for $b_M(x)$. This means that for $x > 100h^{-1}$Mpc the bias is no longer a useful quantity and one should directly work with the halo and matter correlations. In agreement with Desjacques (2008) we find that the two-point correlation of massive halos, that have a large bias, strongly amplifies the baryon acoustic oscillation. In addition we also obtain the modifications associated with primordial non-Gaussianity. The baryon oscillation remains strongly amplified, with a small shift, but somewhat less so for positive $f_{\rm NL}$.

Finally, we used the "linearized" form of the halo two-point correlation to derive the halo power spectrum and the halo bias in Fourier space. We also give a simple recipe that ensures that the halo power spectrum always remains positive (this only differs from the direct prediction by terms of order $f_{\rm NL}^2$ and higher). We obtain a good agreement with numerical simulations, without introducing any free parameter. Moreover, the two formulae described above allow one to estimate the range over which linear approximations over $f_{\rm NL}$ are sufficient. Thus, we find that terms of order $f_{\rm NL}^2$ start playing a role at low k ($k < 0.01h{\rm Mpc}^{-1}$) for large negative $f_{\rm NL}$ ($f_{\rm NL} < -100$), where the direct formula would give a negative power spectrum.

These results, which do not involve free parameters (except for the mass function, if one requires its full shape, where one needs the fit to numerical simulations for Gaussian initial conditions) should be useful to constrain primordial non-Gaussianities from observations of large-scale structures. In particular, as discussed above for Eq.(95), the method presented in this article is quite general and can be applied to a large class of models. Moreover, since it provides results in both real space and Fourier space (i.e. the halo two-point correlation and power spectrum) it gives a complete and consistent description of halo clustering. As for previous approaches, the most reliable use of these models to constrain cosmology is to take advantage of the specific shape of the dependence on mass (for the mass function) or scale (for the bias) brought by primordial non-Gaussianity to constrain $f_{\rm NL}$ (rather than the change in the amplitude at a given mass or scale).

References

Afshordi N., Tolley A.J., 2009, arXiv:0806.1046
Amara A., Refregier A., 2004, MNRAS, 351, 375
Arkani-Hamed N., Creminelli P., Mukohyama S., Zaldarriaga M., 2004, JCAP, 4, 1
Bardeen J., Bond J.R., Kaiser N., Szalay A.S., 1986, ApJ, 304, 15
Barnaby N., Cline J.M., 2006, Phys. Rev. D, 73, 106012
Bartolo N., Matarrese S., Riotto A., 2002, Phys. Rev. D, 65, 103505
Bartolo N., Komatsu E., Matarrese S., Riotto A., 2004, Phys. Rep., 402, 103
Colafrancesco S., Lucchin F., Matarrese S., 1989, ApJ, 345, 3
Dalal N., Dore O., Huterer D., Shirokov A., 2008, Phy. Rev. D, 77, 123514
Desjacques V., 2008, Phys. Rev. D, 78, 103503
Desjacques V., Seljak U., Iliev I.T., 2009, arXiv:0811.2748
Falk T., Rangarajan R., Srednicki M., 1993, ApJ, 403, L1
Grinstein B., Wise M.B., 1986, ApJ, 310, 19
Grossi M., Dolag K., Branchini E., Matarrese S., Moscardini L., 2007, MNRAS, 382, 1261
Grossi M., Verde L., Carbone C., et al., 2009, arXiv:0902.2013
Hamilton A.J.S., Kumar P., Lu E., Matthews A., 1991, ApJ, 374, L1
Kaiser N., 1984, ApJ, 284, L9
Komatsu E., et al., 2008, arXiv:0803.0547
Lucchin F., Matarrese S., 1988, ApJ, 330, L535
Lo Verde M., Miller A., Shandera S., Verde L., 2008, JCAP, 4, 14
Lyth D.H., Ungarelli C., Wands D., 2000, Phys. Rev. D, 67, 023503
Maggiore M., Riotto A., 2009, arXiv:0903.1251
Matarrese S., Lucchin F., Bonometto S.A., 1986, ApJ, 310, L21
Matarrese S., Verde L., Jimenez R., 2000, ApJ, 541, L10
Matarrese S., Verde L., 2008, ApJ, 677, L77
Mo H.J., White S.D.M., 1996, MNRAS, 282, 347
Mo H.J., Jing Y.P., White S.D.M., 1997, MNRAS, 284, 189
Peacock J.A., Dodds S.J., 1996, MNRAS, 280, L19
Pillepich A., Porciani C., Hahn O., 2009, arXiv:0811.4176
Politzer H.D., Wise M. B., 1984, ApJ, 285, L1
Press W.H., Schechter P., 1974, ApJ, 187, 425
Senatore L., Tassev S., Zaldarriaga M., 2008, arXiv:0812.3658
Slosar A., Hirata C., Seljak U., Ho S., Padmanabhan, 2008, JCAP, 8, 31
Valageas P., 2002a, A&A, 382, 412
Valageas P., 2002b, A&A, 382, 431
Valageas P., 2009a, arXiv:0905.1910
Valageas P., 2009b, arXiv:0905.2277